



Calculation of slamming wave loads on monopiles using fully nonlinear kinematics and a pressure impulse model

Ghadirian, Amin; Pierella, Fabio; Bredmose, Henrik

Published in:
Coastal Engineering

Link to article, DOI:
[10.1016/j.coastaleng.2022.104219](https://doi.org/10.1016/j.coastaleng.2022.104219)

Publication date:
2023

Document Version
Publisher's PDF, also known as Version of record

[Link back to DTU Orbit](#)

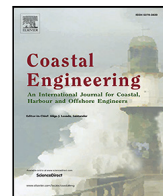
Citation (APA):
Ghadirian, A., Pierella, F., & Bredmose, H. (2023). Calculation of slamming wave loads on monopiles using fully nonlinear kinematics and a pressure impulse model. *Coastal Engineering*, 179, Article 104219. <https://doi.org/10.1016/j.coastaleng.2022.104219>

General rights

Copyright and moral rights for the publications made accessible in the public portal are retained by the authors and/or other copyright owners and it is a condition of accessing publications that users recognise and abide by the legal requirements associated with these rights.

- Users may download and print one copy of any publication from the public portal for the purpose of private study or research.
- You may not further distribute the material or use it for any profit-making activity or commercial gain
- You may freely distribute the URL identifying the publication in the public portal

If you believe that this document breaches copyright please contact us providing details, and we will remove access to the work immediately and investigate your claim.



Calculation of slamming wave loads on monopiles using fully nonlinear kinematics and a pressure impulse model[☆]

Amin Ghadirian^{*}, Fabio Pierella, Henrik Bredmose

DTU Wind Energy, Koppels Allé Building 403, DK-2800 Kgs. Lyngby, Denmark

ARTICLE INFO

Keywords:

Slamming waves
Offshore wind turbine
Wave loads
3D sea states
Directional spreading
Pressure impulse
Force impulse
Wave kinematics
Fully nonlinear
Potential flow
ULS
Ultimate limit state
Offshore

ABSTRACT

The design methods for highly nonlinear wave loads on monopile structures has over the past years been extended with methods based on pre-computed fully nonlinear wave kinematics. Yet, the slamming events of the strong sea states cannot currently be predicted with these methods. We here present a simple recipe for the application of a recent pressure impulse based slamming load model in combination with fully nonlinear wave kinematics and validate the results against lab measurements of uni- and multi-directional storm sea states. The experimental slamming loads are extracted from lab measurements equivalent to 954 full scale hours. Six methods for the extraction of the slamming force are developed and analysed in detail, with a final selection of two for the further analysis. The experimental analysis shows that the frequency of slamming is larger in uni-directional sea states relative to sea states with directional spreading, and with slightly smaller force impulses.

The calculated slamming frequencies from the measurements are used in the application of the numerical slamming model. It is shown that the application is straightforward and robust and involves an intuitive selection of the model inputs from the incident wave kinematics. A generally good agreement between the model and measurement distributions of the force impulse is observed. The difference between 3D and 2D slamming impulses, though, is found to be larger in the numerical model. This is traced to the numerical particle velocities in the wave crests.

The pressure impulse model is next extended by assuming a predefined generic slamming force time variation and through calibration of the peak slamming force, a generally good agreement between the model and ensemble-averaged measured slamming force time series is obtained, given the uncertainty in the slamming load extraction. It is also observed that the commonly used non-dimensional slamming force peak of 2π is unrealistically large in the irregular slamming waves because of the 3D effects of small curling factors.

1. Introduction

In the design process of offshore wind turbine substructures, the slamming wave loads are one of the steps associated with the largest uncertainties. For a precise reproduction of a slamming wave event, it is necessary to either perform experiments or to use detailed viscous solvers. For example, Bredmose and Jacobsen (2010, 2011), Hildebrandt and Schlurmann (2012), Östman et al. (2015), Jose et al. (2016a), Ghadirian et al. (2017), Veic and Sulisz (2018), Liu (2019) have used Computational Fluid Dynamics (CFD) for calculating the slamming wave loads on offshore wind monopiles. However, for design purposes, it is usually desirable to predict the slamming loads from wave field parameters that are known in advance. A designer needs

two main inputs, namely kinematics of the underlying wave field and a slamming load model. Pierella et al. (2021c) suggested a method for using a database of pre-computed fully nonlinear wave kinematics for achieving accurate loads while avoiding the high computational cost of running fully nonlinear wave models. For the second input, several engineering slamming load models are available. However, since these methods usually try to predict the details of the slamming wave force time series based on theories of still water entry of a 2D cylinder, the uncertainty of these models is relatively large (Hallowell et al., 2016). The main objective of this paper is to address this challenge by providing a new method for calculating the force impulses of the slamming waves, based on wave kinematics of a fully nonlinear potential flow solver.

[☆] This document is the results of the research project funded by the Innovation Fund Denmark and other partners as part of DeRisk project with grant number 4106-00038B.

^{*} Corresponding author.

E-mail address: amgh@dtu.dk (A. Ghadirian).

<https://doi.org/10.1016/j.coastaleng.2022.104219>

Received 27 August 2021; Received in revised form 17 September 2022; Accepted 25 September 2022

Available online 30 September 2022

0378-3839/© 2022 The Authors. Published by Elsevier B.V. This is an open access article under the CC BY license (<http://creativecommons.org/licenses/by/4.0/>).

One of the most widely used methods for calculating the slamming forces on offshore wind turbines is based on the work by Goda et al. (1966)

$$F_I(t) = \lambda \eta_b C_s \rho R C^2 \left(1 - \frac{C}{R} t\right), \quad (1)$$

where λ is the curling factor, η_b is the free surface elevation of the slamming wave, ρ is the water density, R is the cylinder radius and C is the celerity of the wave. The equation is applied in the time interval from 0 to R/C . In this model, C_s , commonly known as the slamming coefficient, is equal to π based on the theory developed by von Karman (1929). The developed theory, though, did not consider the pile-up effect from the displaced water when an object enters a flat water surface.

Wagner (1932) developed a model in which the pile-up effect was taken into account, resulting in $C_s = 2\pi$. Wienke and Oumeraci (2005) later used Wagner's theory and developed a model that takes into account the angle of the cylinder relative to the wavefront while assuming a uniform slamming force over the length of the impact zone on the cylinder. Most recently, Paulsen et al. (2018) suggested an empirical model that showed better agreement with experiments than the previously existing models. For a more thorough summary of the literature about this topic, the reader is referred to Ghadirian and Bredmose (2019b).

The mentioned models considering the slamming force on offshore wind turbines focus mostly on the peak value of the slamming force and show varying consistency with experiments (Hallowell et al., 2016). Since the duration of the slamming event is usually short compared to the first natural period of the offshore wind turbine sub-structures, the exact peak value is not essential for the response calculations and calculating the force impulse instead of the slamming force time series, is often sufficient. Force impulse, as an integrated quantity, can be expected to have a lower uncertainty and also a closer link to the parameters of the incident wave. Therefore, in this paper, a simple recipe for the application of a slamming force impulse model is proposed, driven by stochastic time series of fully nonlinear wave kinematics.

The methodology is based on the Pressure Impulse (PIMP) model, developed by Ghadirian and Bredmose (2019b) and fully nonlinear kinematics from a potential flow solver, OceanWave3D (Engsig-Karup et al., 2009), as inputs. The PIMP model was previously validated against one CFD reproduction of a slamming wave on a cylinder in Ghadirian and Bredmose (2019b); against laboratory measurements with inputs from the same measurements in Ghadirian and Bredmose (2019a); against measurements with inputs from the OceanWave3D reproductions of two irregular sea states in Pierella et al. (2019) and against CFD simulations of slamming waves on a vertical surface piercing cylinder with inputs from OceanWave3D in Ghadirian and Bredmose (2020a). In Pierella et al. (2019) and Ghadirian and Bredmose (2020a), a similar, yet preliminary, implementation of the proposed methodologies of the current paper was presented. The current work, however, broadens the mentioned studies in the parameter domain and extends and refines the procedure to compute the slamming loads from numerical simulations.

First, we propose and validate a methodology to separate the pressure impulse from 134 h of experimental wave and force data, equivalent to 954 h at full scale. Second, we derive a simple and robust methodology to compute the pressure impulse from fully-nonlinear statistical reproductions of the DeRisk tests, and we perform a thorough validation against the experimental force impulses mentioned above. Third, we present a clear methodology to determine the time series of the slamming load force from the computed pressure impulses.

In Section 2, the methodology of identifying the slamming waves on the cylinder from lab measurements and isolating the slamming part of the force time series is described. Since this can be a subjective task, six independent methods are evaluated and compared in terms of the statistical distribution of the force impulses for 2D and 3D sea

states. Two methods are next chosen for the further analysis. This is, to the best of the authors' knowledge, the most extensive study on this topic in the literature until now. Afterwards, in Section 4, the models for calculating the wave kinematics and the pressure impulses are explained. The methods for choosing the potentially slamming waves from the kinematics and calculating the force impulse (FIMP) are elaborated and the resulting distributions of the force impulses are presented and compared to those of the measurements.

In an additional step, in Section 5, a method for calculating slamming force time series from the model results is proposed using a general form time series. The peak slamming force value from the literature is used while considering the effect of the overturning height of the slamming wave on it. This effect is investigated theoretically. The resulting slamming force time series from the measurements and model results are presented and their peak value and period statistics are studied thoroughly. The possible inclusion of the new method in design is discussed in Section 6. In the last section, Section 7, conclusions are drawn from the findings and the significance of the results are stated.

2. The experiments and identification of the slamming events

In this section, the experiments and methodology for the identification of the slamming wave episodes are presented.

2.1. The experiments

The experiments were conducted at DHI Denmark in 2015 as part of the DeRisk project (Bredmose et al., 2016), at a scale of 1:50. All measures in this section, though, are given at full scale, except when specified. A top view drawing of the wave basin layout is shown in Fig. 1, with the wave paddles shown with a red hashed rectangle and the location of the cylinder shown with a red square.

Random realizations of irregular waves in 25 different sea states with a JONSWAP spectral power density were used. The sea states are shown in Table 1. The water depth in the tests was either 20 m or 33 m while the tests included sea states with and without directional spreading. In Table 1, in addition to the case number and the water depth, the nominal significant wave height (H_s), peak period (T_p), directional spreading parameter s , peak enhancement parameter (γ) and the return period of the tested sea states are presented. The directional spreading parameter, s , was used to generate the \cos^{2s} distribution (Miles and Funke, 1989), from which the random directions were sampled. These sea states and water depths were chosen as relevant conditions for Ultimate Limit State (ULS) load cases in the North Sea (Bredmose et al., 2016) with return periods from 10 to 1000 years.

The tests were conducted in a wave basin with 36 wave paddles. A cylinder was installed 7.3 m (model scale) from the wave paddles (see Fig. 1), and it was attached to the basin floor and to an upper supporting structure via two force transducers. The inline force was measured using these two force transducers with a 180 Hz sampling frequency. The structure eigenfrequency was well above the range where the wave energy was concentrated, therefore its response was easily separable via Butterworth low-pass filtering. The force time series were first low-pass filtered with a high-cut frequency of 3 Hz. The free surface elevation, η , was measured using 31 wave gauges around the cylinder and extending towards the wave paddles. However, for the current work, only η at the centre of the cylinder was used for reproducing the forces. In the cases without directional spreading, we measured the free surface elevation η by a wave gauge positioned 0.2 m distant cross-flow from the cylinder (model scale). For the sea states with directional spreading, for each time step, we interpolated the free surface elevation η measured by 5 wave gauges around the cylinder, excluding the wave gauges that were in the wake of the cylinder, positioned 0.2 m from the cylinder respectively in the x and y directions.

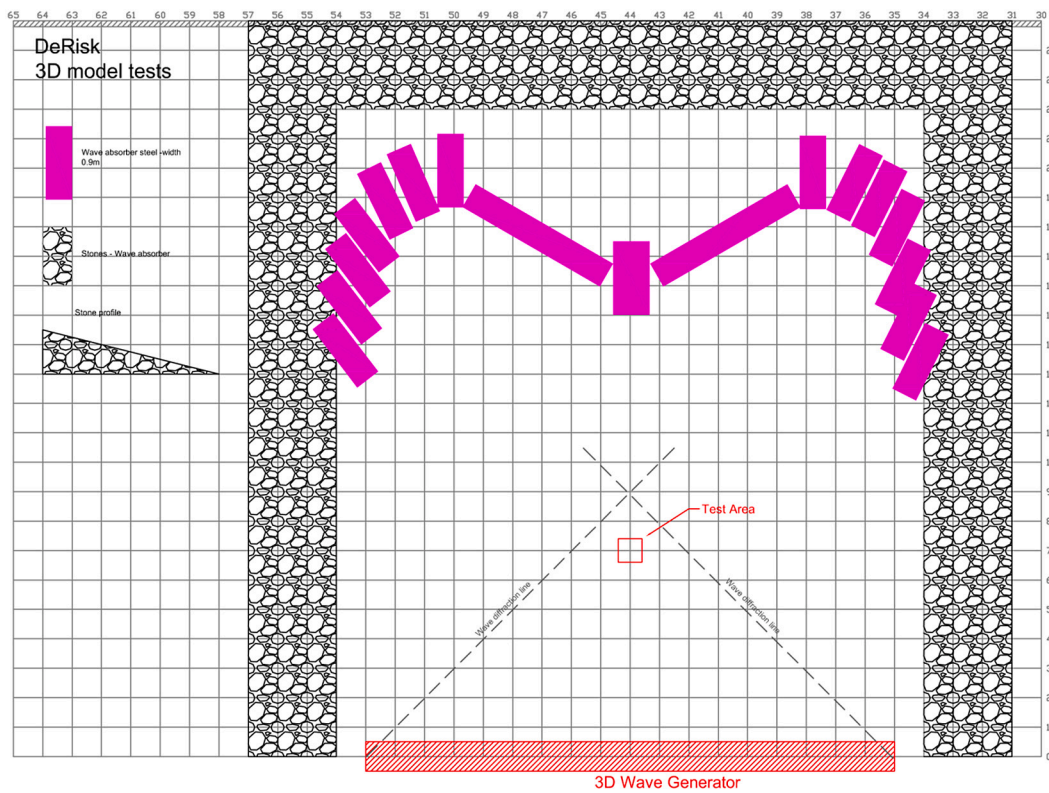


Fig. 1. A top view drawing of the test basin (Bredmose et al., 2016). Dimensions in the drawing are at model scale (1:50 with respect to full scale).

Table 1
Characteristics of the investigated sea states (full-scale values).

Case number	Depth [m]	H_s [m]	T_p [s]	s [-]	γ [-]	Spreading	Return period [year]
1	33	8.5	13.5	0	1.5	2D	10
2	33	8.5	13.5	13	1.5	3D	10
3	33	8.5	13.5	5	1.5	3D	10
4	33	7.5	12	13	2.0	3D	10
5	33	7.5	15	13	1.0	3D	10
6	33	9.5	12	13	3.6	3D	100
7	33	9.5	15	13	1.2	3D	100
8	33	11	15	13	1.7	2D	1000
9	33	7.5	12	0	2.0	2D	10
10	33	7.5	15	0	1.0	2D	10
11	33	9.5	12	0	3.6	2D	100
12	33	9.5	15	0	1.2	2D	100
13	33	11	15	0	1.7	2D	1000
14	20	5.8	12	13	1.0	3D	10
15	20	5.8	15	13	1.0	3D	10
16	20	6.8	12	13	1.6	3D	100
17	20	6.8	15	13	1.0	3D	100
18	20	7.5	15	13	1.0	3D	1000
19	20	5.8	9	13	4.3	3D	1000
20	20	5.8	12	0	1.0	2D	10
21	20	5.8	15	0	1.0	2D	10
22	20	6.8	12	0	1.6	2D	100
23	20	6.8	15	0	1.0	2D	100
24	20	7.5	15	0	1.0	2D	1000
25	20	5.8	9	0	4.3	2D	1000

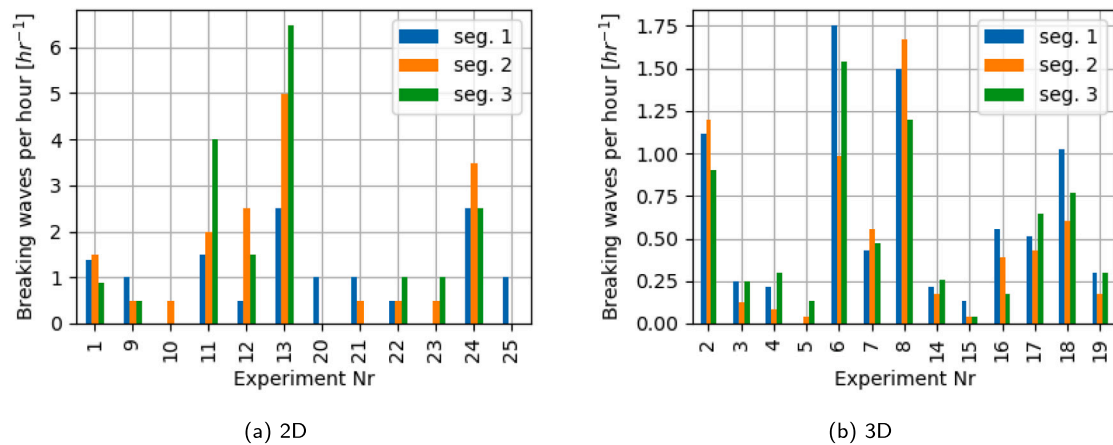


Fig. 2. Number of breaking events per hour when subdividing the experimental time series in three segments for 2D sea states (left) and 3D sea states (right).

Due to the long duration of the experiments, and as no active absorption techniques were used in the experiments, standing waves can build up in the basin due to wave reflection, which could possibly modify the wave field in the basin. It was therefore decided to check whether the statistics of the slamming events are constant with time. To this end, the acquired time series were subdivided in three segments of equal length, and for each segment, the number of breaking events was counted and divided by the length in hours of the segment. The results, in Fig. 2, do not show a substantial increase of the breaking intensity for any of the 3D experiments. In two of the 2D experiments (number 11 and 13), though, the rate of slamming events is increasing with time. As they are the two sea states with the highest steepness, this could be associated with a build-up of low-frequency energy in the wave tank, where the wave absorbers used in the current experiments could be less effective. However, from the frequency spectra of the free surface elevation measured in different locations of the domain (see f.ex. Figures 6 and 7 in Pierella et al. (2021a)), no significant build-up of energy below the peak period was observed.

A further check was made with respect to the force impulse magnitude. It was observed that the magnitude of the force impulses associated with the slamming events did not grow with time. Although it is desirable to achieve a constant slamming rate in time, the non-changing behaviour of the force impulses suggests that the nature of the slamming events did not change. We therefore decided to keep sea state 11 and 13 within the analysis. We note here, that in this study we do not aim to develop a method to predict the slamming rate in time, but rather to predict the magnitude of the slamming force. Estimates for the slamming rate, may be based on methods from the literature as Paulsen et al. (2018), Dawson et al. (1993).

For completeness, in Section 3.2 of this manuscript we briefly explore the sensitivity of the current analysis to the events in the last part of simulations 11 and 13, that were the most affected by the increase in slamming rate.

2.2. Identification of the slamming waves

To validate the force impulses and slamming time series calculated by the model, the slamming wave events were identified by a screening process of the inline force time series. The identification is not trivial and, if accurate tests are not performed, can be subjective.

Many methods to identify slamming events from time series of measurements have been used in the literature. For example Alsalah et al. (2021), identified slamming events on a ship by analysing the accelerations signal from the accelerometers positioned on the shipbow. Through the empirical mode decomposition analysis (EMD, see Huang et al. (1998)), the accelerometer signal was divided into modes, that

were classified either as quasi-static or dynamic depending on their frequency content. When the dynamic modes contained a significant part of the total energy, a slamming event was identified. The applicability of methods based on the analysis of the acceleration depends heavily on the eigenfrequency of the analysed structure. When applied to flexible cylinders, the fore-aft eigenfrequency may be too close to the wave excitation frequency, and be therefore excited also by nonbreaking waves (Stansberg et al., 1995). In very stiff structures, like the one in this work, the fore-aft eigenfrequency could be hard to excite by the smallest slamming events.

A further possibility to identify slamming waves is to analyse the signals from pressure transducers installed on the surface of the cylinder. When a pressure peak is registered in one of the sensors, there is a high chance that the peak is caused by a breaking wave. Vestbøstad et al. (2017) successfully used arrays of pressure sensors to identify slamming loads on the columns of a TLP oil platform in a wave tank experiment. In the current experiments, five pressure sensors were installed at the upstream centre line of the cylinder (Dixen, 2019). However, when analysing the time series of the pressures in different sea states, there seemed to be no obvious peak pressure value beyond which the wave could be reliably considered as breaking. This could be related to the 8[m] coarse spacing between the pressure sensors, which meant that waves impacting the cylinder in between the pressure sensors would be unnoticed by this technique.

Visual identification is also a possibility, if video recordings of the experiments are available. Suja-Thauvin et al. (2017) have used videos of irregular realization of 2D waves to identify breaking waves. The criterion was based on the manual identification of lateral and vertical ejection of water particles when a breaking wave impacted on the cylinder. Although this method has the potential to be quite precise, it can also be subjective. Moreover, it heavily relies on the quality of the videos. Especially in 3D irregular sea states, where the reflection of light is uneven due to the three dimensional wave crests, this criterion may be more difficult to apply. In the current work, visual identification of breaking waves from the videos was actually used to validate the slamming identification. However, due to the length of the time series and to the non-optimal illumination of the free surface, it was not used as the main criterion, but as a spot check of the slamming events identified by analysis of the force time series.

Another possibility for slamming detection is to analyse the time series of loads and free surface elevation. In particular, a slamming load event would be associated with a steep free surface elevation signal and by a sudden increase in the slope of the force signal. Paulsen et al. (2018) observed that slamming events are characterized by a significant increase in the loads in a time scale that is significantly lower than the time scale of an average wave. Therefore, they first identified peaks from the force time series peaks that were larger than 3 times the

standard deviation of the total time series. If the increase happened in a time span $\tau < \frac{1}{8}T_p$, where T_p is the peak period of the analysed sea state, then a slamming event was identified. This algorithm, however, has some shortcomings when identifying smaller spilling breakers that generate small force peaks, although this is justified by the fact that their impact on the load statistics is moderate.

Based on the above considerations, we decided to rely on a similar methodology for the identification of breaking waves, combined with the observation of the recorded videos of the experiments for validation. After a thorough investigation, we found that a robust identification can be achieved by satisfying four criteria. To begin with, breaking waves had inline force peak values larger than ρghR^2 . This made sure that we identified the waves that induced large forces, which are more important in the design process. Furthermore, we selected waves where the time derivative of the inline force had peak values larger than $10\rho ghR^2/T_p$. This empirical condition made sure that the force time series had a slamming part which induced a sudden increase in the inline force. The threshold of the force peak value and its time derivative were chosen empirically. In addition, the selected wave episodes had to be separated by at least one peak period, T_p , to make sure that each slamming wave episode was counted only once. Lastly, the force time series had to show a sudden change of slope before it peaked. In the last step, we conducted a visual inspection of the force time series of the selected wave episodes. The slamming events from the previous criteria were then looked up in the video footage of the experiment, and it was checked that the waves were actually breaking.

Using this method, 117 slamming wave events were identified from 90 h of irregular uni-directional (2D) sea states and 487 from 864 h of irregular multi-directional (3D) sea state experiments. This corresponds to an average of 1.3 slamming waves per hour in the 2D sea states and 0.56 slamming waves per hour in the 3D sea states. We believe that the reason for the larger slamming frequency in the 2D sea states than in the 3D sea states lies in the mechanisms that lead to the generation of large waves. Let us consider two sea states (2D, 3D) with the same H_s and T_p in a fixed location. In a 2D sea state, all waves come from the same direction with different speeds. Ultimately, the faster waves catch up with slower waves and slowly superpose to generate large waves (dispersion focusing). In a 3D sea state, in addition to the dispersion focusing, a second mechanism is present. Waves that come from different directions can superpose to generate a large wave quite rapidly. This is called directional focusing. The difference in the speed of the two physical processes with which large waves are created makes breaking and overturning of the waves more probable in the 2D sea states, where nonlinear interactions have more time to develop and where the breaking is likely to have longer duration and thus longer extent in space.

To check that the identification of the breaking waves was successful, we extracted the period T of all of the single wave events from the time series of the experimental tests by using successive zero downcrossings of the free surface elevation signal. The height H of each event was computed as the difference between the maximum and the minimum free surface elevation within two successive zero downcrossings. From each event, a nondimensional height $H/(gT^2)$ and depth $h/(gT^2)$ was plotted in Fig. 3 together with Goda (2010)'s breaking criterion for two values of the breaker index constant, $A = 0.12$ and $A = 0.18$, which mark the area where irregular waves are likely to break. The results show how the identified slamming waves are indeed concentrated in the area close to the breaking limit, which supports the soundness of the current identification method.

3. Isolation of the slamming force time series

After identifying the slamming waves on the cylinder from the measurements, we isolated the slamming force time series from each event. This separation is based on the hypothesis that the total inline force is a superposition of the slamming and the non-slaming parts,

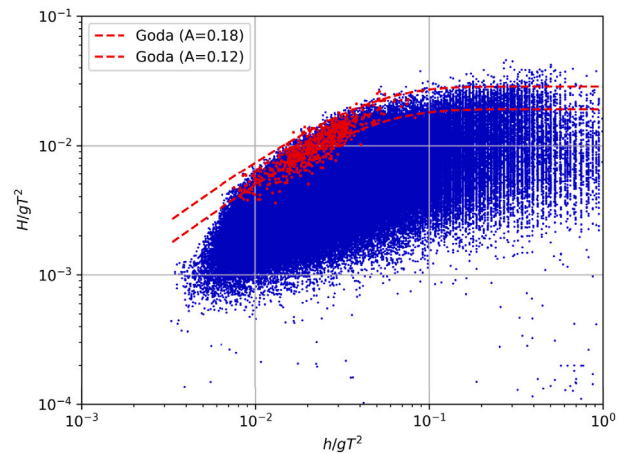


Fig. 3. Single wave events from all of the experiments in Table 1. Non-breaking waves are represented with a blue marker, while breaking waves are represented with a red marker. The two dashed lines represent the breaking criterion from Goda (2010) with two values of the proportionality coefficient $A = 0.12$ and $A = 0.18$.

which is a widely used assumption in this field (see e.g. Goda et al. (1966) and Wienke and Oumeraci (2005)).

Some approaches to isolate the slamming force from a time series of a wave slamming event have been proposed in the literature. Irschick et al. (2004) used a combination of the EMD and low-pass filtering to decompose the force time series into a dynamic and a quasi-static contribution. Afterwards, they used a dynamic numerical model of the structure to reconstruct the slamming load that would generate the observed dynamic forcing. Wienke and Oumeraci (2005) uses a similar method, where the dynamic contribution is obtained by the subtraction of the force history of the quasi-static load generated by a non-breaking wave from the time history generated by a breaking wave impact, therefore including both the quasi-static load and the dynamic load. Once the dynamic load is available, the actual total force is obtained by a deconvolution followed by a convolution operation with a predetermined load time history. Both methods cannot however be used in our work, since due to the high natural frequency of the cylinder, the dynamic loads associated with the smallest slamming events can be hard to detect. In a subsequent study, Irschick et al. (2011) suggested to use the Hilbert Transform to identify the point in which the phase velocity of the wave deviates significantly from the expected phase velocity based on the wave period, estimated via either the peak period of the sea state T_p or the zero-crossing period T_z . However, the method is based on free surface elevation measurements at the cylinder location. While this is simple to achieve with 2D waves using a wave gauge on the side of the model cylinder, this cannot be achieved with 3D waves unless the experiments are repeated without the cylinder, which was not the case in the current experiments. For this reason, this method could not be applied in the current study.

3.1. Six methods for extraction of the slamming force

Due to the lack of appropriate separation methods for the current case, we decided to develop six in-house methods. to isolate the slamming wave loads from the background irregular wave forces. They are detailed in the rest of this section. To compare their performance, in Fig. 4 we show the application of the methods to the force time series from one example event. The time series including slamming are shown with solid black lines and the non-linear non-slaming time series are shown with dashed black lines. The slamming event is visible with a sudden change in the slope of the time series at around 185,909 s, a

turning point, just before the signal peaks. The time series also shows the Secondary Load Cycle in the local minimum preceding the peak of the time series, see for example Grue et al. (1994) and Ghadirian and Bredmose (2020b).

For comparisons purposes, in Fig. 5, we provide the distribution of the normalized force impulses computed via the 6 methods for all of the slamming events in the 2D and 3D sea states. This information is hereafter used to assess the performance of the different methods.

Method 1: Quadratic polynomial fit (QP): The intuition behind this method comes from the observation that the quasi-static load time series has a smooth shape. If the starting and ending point of the slam load cycle can be identified, we can fit a second-order polynomial. A quadratic polynomial was chosen so that the resulting time series could include some of the non-linearity of the non-slaming force signal. This was considered a superior methodology to the simpler solution of fitting a straight line through the identified points. This method has not been used before to the knowledge of the authors.

First, we selected the inflexion point (zero second derivative) of the in-line force time series just before the main peak. We call this point P_1 . This is the point where the slope changes sign, and therefore marks the likely insurgence of a slam load event. Afterwards, we chose a second point after the peak of the force time series with the same force value as the first point, denominated P_2 . Knowing the time instants for P_1 and P_2 , the associated force values, and the slope of the force time series at P_1 , a quadratic polynomial fit through the two points is done. Note that using this method, the slope of the fitted parabola at point P_2 is not required to match the slope of the original force time series. This could be theoretically achieved using a cubic polynomial. However, this methodology was found to typically produce peaks larger than the original signal, and was therefore abandoned.

An example of the application of the QP method is shown in Fig. 4(a). The grey shaded area shows the separated slamming force impulse. The non-slaming time series consists of the original time series outside of the range of the fit and of the quadratic polynomial fit itself. As expected, this time series is not smooth as the slope of the time series changes suddenly at the second intersection between the quadratic polynomial and the original time series. In Fig. 5(a), the histogram of the impulses extracted by all the time series via this methodology is plotted. We can see how the method returns a high probability of having close to zero force impulses.

Method 2: Improved quadratic polynomial (ImpQP): The second method was very similar to the first method, however the second selected point on the force time series was chosen so that the slope of the polynomial would have less than 10% relative difference with the slope of the original force time series. This method ensured smoother non-slaming force time series, which is believed to be more physical by the authors. This method is also novel to the authors' knowledge, and no reference were found in the literature.

In Fig. 4(b), an example of the usage of this method is shown. With respect to Fig. 4(a), the non-slaming time series in this plot is smoother and the slamming part is separated less sharply. A sudden change of the slope of the non-slaming force time series is less physical. This is a clear advantage of ImpQP method compared to QP method. Moreover, in this particular case the duration for the slamming impulsive load was greater than for the QP method, due to the more strict criterion applied to the slope. This is also visible in Fig. 5(b), where the histogram of the impulses extracted is wider than for the QP method, and as a result, the distribution is less skewed towards the zero. Because of the clear advantage of the ImpQP method to the QP method, only the improved one was used in the further analysis.

Method 3: Aggressive filtering (AggFil): A commonly used method for isolating the slamming force time series in the literature is the application of aggressive filtering of the force time series, see e.g. Paulsen et al. (2018), Jose et al. (2016b) and Hansen and Kofoed-Hansen (2017). This method was used here with a Butterworth 3rd order filter with a high-cut frequency of $5 \cdot f_p$, where f_p is the peak frequency of the corresponding sea state. Even though the forward-backwards filtering (Gustafsson, 1996) was used to avoid phase shifting, we realigned the filtered signal and the original signal by finding the maximum correlation between the two signals in the interval of each slamming event. This method is denominated AggFil hereafter and an example application of it can be seen in Fig. 4(c). In this example, the aggressive filter smooths the time series significantly. The slamming load is then identified by the upcrossing and successive downcrossing of the original and of the smoothed signal. In this case, the start of the force impulse does not match with the sudden slope change of the force signal. Moreover, the quasi-static force in this method does not match closely the force time series of the non-slaming signal. This would be a required feature, since otherwise there is the risk of over or underestimating the force impulse, which is computed using the difference between the original and the filtered time series. The statistics of the method is reflected in Fig. 5(c), where the distribution of the force impulses is quite narrow, and centred at about $0.1 FI / (\rho R^2 U_{p,linear})$.

Method 4: Variational mode decomposition (VMD): Empirical Mode Decomposition (EMD) (Huang et al., 1998) is occasionally used for isolating the structural response contribution in the total measured force (see e.g. Jose et al. (2016b) and Alsalah et al. (2021)). The objective of the EMD method, in such cases, is to separate the signal into time dependent intrinsic modes. This objective has similarity to the objective of separating the slamming wave force part of the time series from the total measured force time series, although the slamming force itself may be different in nature from a dynamic structural response. The method, however, has a few limitations, mainly a sensitivity to noise and sampling, and that it cannot separate the signal into intrinsic modes when their frequencies are too close. When using the method in the current work, these weaknesses were also apparent, and led to an early dismissal of the method.

To address these limitations, extensions of the EMD method have been adopted. For example, Spinosa and lafrati (2022) used the Ensemble Empirical Mode Decomposition (EEMD) to reduce the mechanical electric noise contribution in impulsive force measurements from airplane and helicopter emergency water entry. The Variational Mode Decomposition (VMD) method, developed by Dragomiretskiy and Zosso (2014), divides the signal into an ensemble of band-limited amplitude and frequency modulated intrinsic modes. We here adopt this method to divide the signal into 5 modes and chose the last mode as the slamming force part of the signal. Even though the narrow-band assumption behind the VMD method would result in the separated modes differing from the true slamming and non-slaming signals, the conducted visual tests showed reasonable resulting signals. An example of the application of this method is shown in Fig. 4(d). In this particular example, the VMD methodology returns a smaller impulse than e.g. the ImpQP method, and a quite similar impulse to the AggFil method. This is also reflected in Fig. 5(c) and (d), which show quite similar force impulse distributions for the two methods.

Method 5,6: Stokes expansion around linear force and free surface elevation (StExpF and StExp η): The last two methods were based on the assumption that there is a Stokes-type perturbation expansion for a wave group for both free surface elevation (η) and force (F), see e.g. Walker et al. (2004), Fitzgerald et al. (2014) and Chen et al. (2018). By calculating the Stokes-like coefficients we calculated the higher harmonics of the linear irregular force and η time series. To calculate such Stokes-like coefficients we firstly used wave averaging of the original force and η time series based on their respective linearized signals. Ultimately this process resulted in nonlinear (up to the fifth harmonic) non-slaming

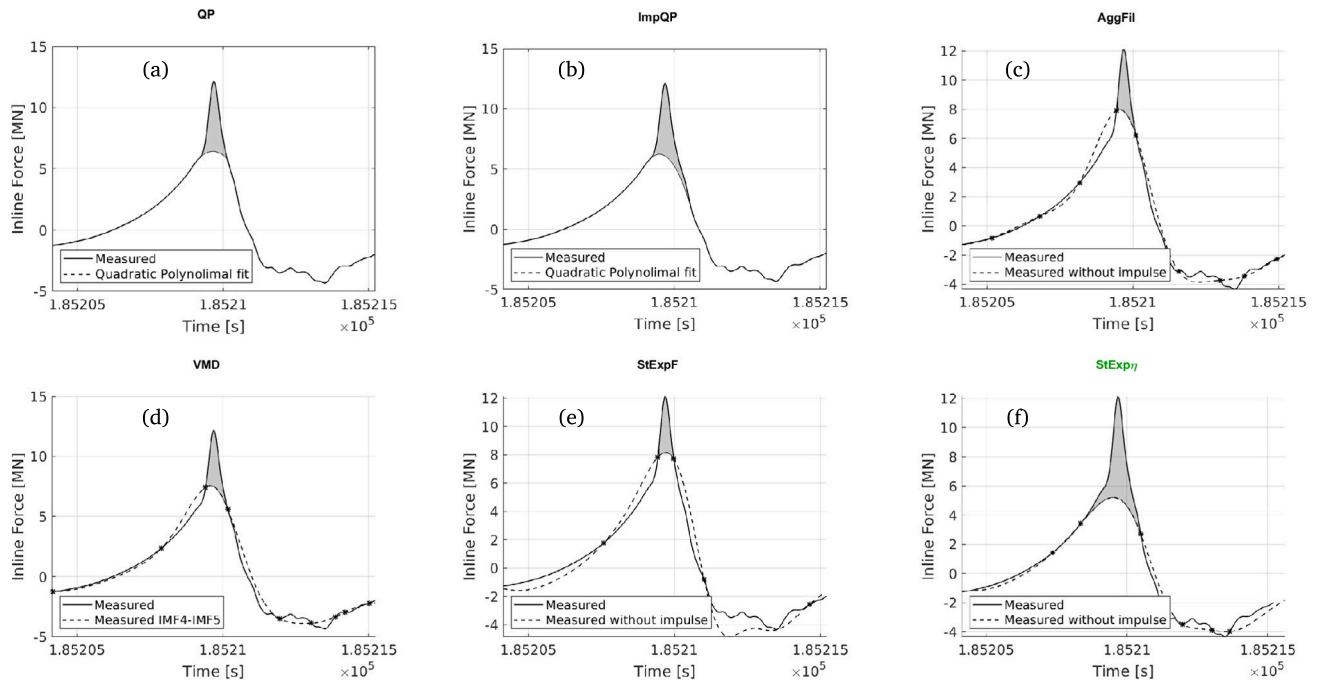


Fig. 4. Application of 6 methods for isolating the non-linear non-slamming inline force time series for an event in sea state 2. The title of the plot using the **StExp η** method is coloured green to indicate the lowest error between the non-slamming and original time series between all the last four methods.

inline force time series that were used to isolate the slamming force signals. This process and the process of calculating the Stokes coefficients are thoroughly explained in Ghadirian et al. (2021). The only extension of the current work compared to Ghadirian et al. (2021) is that here we used the Stokes-like coefficients to calculate the nonlinear irregular force time series and afterwards isolate the slamming force time series while Ghadirian et al. (2021) used the coefficients to calculate the wave-averaged force time series.

The results using the Stokes expansion over linear force and η methods are referred to as **StExpF** and **StExp η** hereafter. Examples of the application of these methods in are provided in Figs. 4(e) and 4(f). The **StExp η** method returns a better match of the quasi-static force part with the original time series in this case. As mentioned above, this is desirable, to be able to extract the most accurate possible force impulse. Moreover, comparing the two methods, one can observe that the force impulse predicted by the Stokes' expansion on the force signal is lower than the one predicted by the same method applied to the free surface elevation signal. This is confirmed by the analysis in Fig. 5(e) and (f), where indeed the extracted impulse for the **StExp η** has a longer tail than for the **StExpF**.

3.2. Final choice of extraction method

From the analysis of the histograms in Fig. 5, we can observe that although the histograms for the different methods have varying widths, quantified by the standard deviation in Table 2, they are in broad agreement with respect to the median impulse, which is approximately between 0.36 and 0.48. The only method which seems to disagree is the **StExp η** , which predicts a higher median impulse. This is intuitively seen also in Fig. 4 where the **StExp η** predicts the largest force impulse.

We now proceed to select the best method that allows to extract the force impulses with the largest accuracy. This choice can be rather subjective, due to the lack of a reference answer for comparison. Hence we based it on a wish for a robust detection method with results that appear physically sound. We chose to prefer the methods that change the force history before the slamming the least. This is based on the observation that the occurrence of a slamming event creates

Table 2

Statistical properties of the histograms in Fig. 5. All quantities in the table are nondimensionalized according to $F_{imp}/(\rho R^2 U_{p,linear} H_S)$.

Method	Mean	Std	Median
QP	0.384	0.364	0.275
ImpQp	0.642	0.747	0.477
AggFil	0.386	0.141	0.360
VMD	0.490	0.134	0.471
StExpF	0.470	0.245	0.446
StExpEta	1.289	0.540	1.175

an impulsive load, which does not alter the past load history. This observation is consistent with the superposition hypothesis that is at the base of the analysis performed in this paper, for which the slamming force can be seen as an independent load contribution on top of the background quasi-static load history.

The **QP** and **ImpQP** are the only two methods that, due to their formulation, leave the pre-slamming force history unchanged. As discussed earlier, we see the **ImpQP** to be superior, and decided to bring it forward in the analysis, at the expense of the **QP**. As for the other 4 methods, they either need to filter the original time series or to reconstruct it in a simplified way, and therefore change the pre-slamming load history. Depending on the shape of the force history, the different models show a different ability to correctly identify the force impulse from the background time series. Hence, we decide to combine the **AggFil**, **VMD**, **StExpF** and **StExp η** into a single method, the **Comb** method. For every impact, we then choose the identification method that shows the lowest error with respect to the pre-breaking force time series. For this purpose, we define the error measure as

$$\epsilon = \frac{\|F(t) - F_{ns}(t)\|}{\|F(t)\|} \quad \text{for} \quad t_{zdc} < t < \max\{t_{inf}, t_{ins}\}, \quad (2)$$

where ϵ is the relative error, $\| \cdot \|$ denotes the Euclidean norm, t_{zdc} is the zero down-crossing instant of the wave episode, t_{inf} is the inflexion instant of the original force time series and t_{ins} is the intersection instant of the original and the non-slamming time series. Thus for each

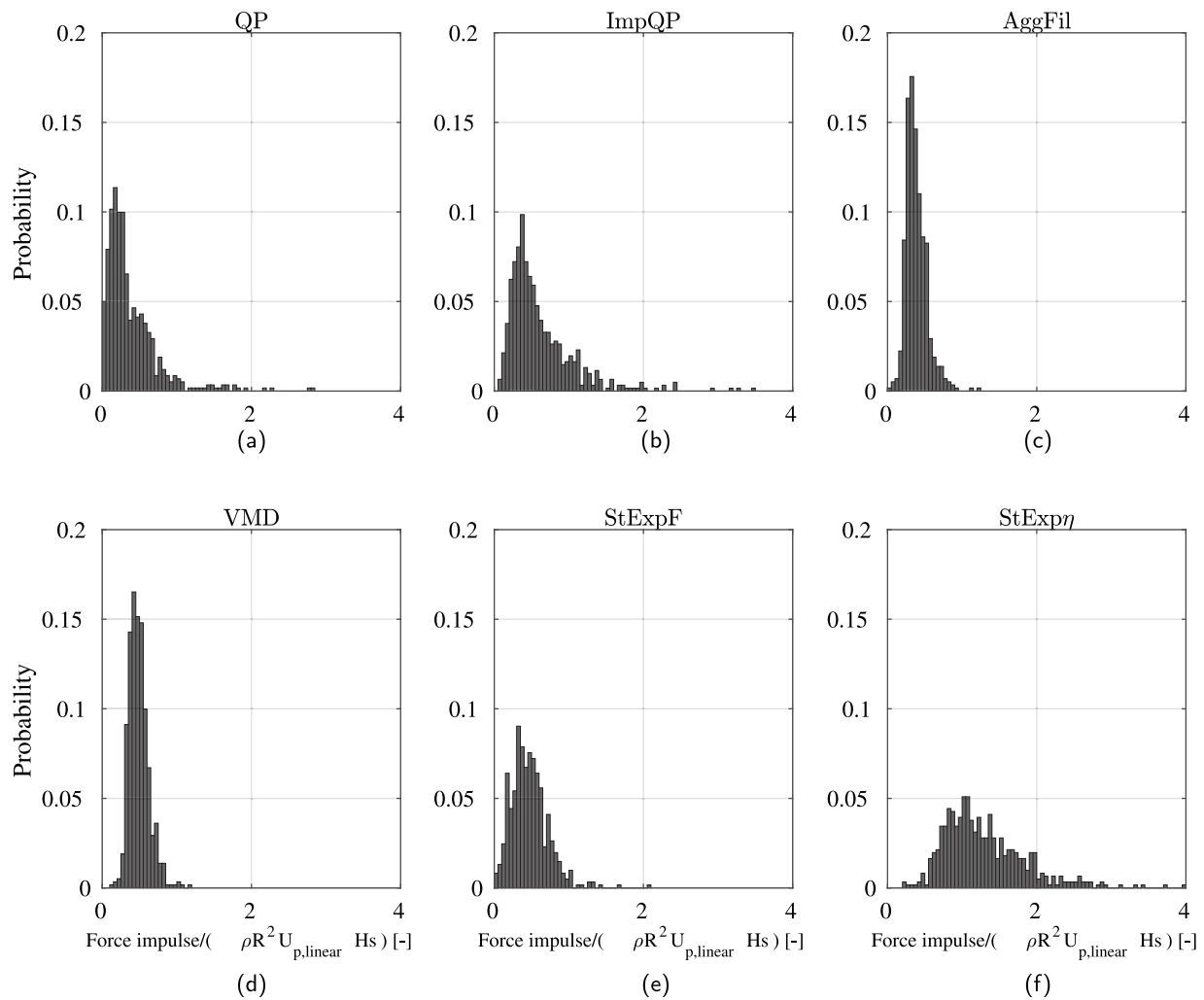


Fig. 5. Application of 6 methods for isolating the non-linear non-slamming inline force time series for all the events in the 2D and 3D sea states.

slamming event, the combined method **Comb** detects the slamming impulse from the method that produces the smallest value of ϵ .

As mentioned above, the relative error was only calculated in the part of the signal preceding the slamming part. The reason behind this is that, for large waves, the Secondary Load Cycle (Ghadirian and Bredmose, 2020b) appears after the peak of the inline force time series, and since it is not reproduced by our methods, it artificially increases the error between the reproduced and the original non-slamming part of the signal.

To conclude this section, we follow up with the discussion in Section 2.2, and assess the effect of the increase of slamming frequency observed in the last segment of sea state 11 and 13. The analysis leading to Fig. 5 was repeated with the events from the last third of experiments 11 and 13 removed. Out of the 15 slamming events in sea state 11, 8 were removed, while out of the initial 28 events in sea state 13, 13 were removed. This leads to an increase in mean and medians of about 6% for the 2D events and 1% for the full set of 2D and 3D events. On this basis we conclude that the presented analyses based on the full set of events are robust enough to draw meaningful conclusions.

3.3. Extracted slamming force time series and force impulses from the measurements

It was observed, after selecting the isolating method for all of the events for the **Comb** method that more than 70% of the events were isolated using **VMD**, more than 15% **AggFil**, 2% from the **StExpF**, 10%

from **StExpeta**. Generally, the events with the largest inline force peaks were isolated best using the **StExpeta** method and the events with the smallest inline force peaks were isolated best using the **AggFil** method.

The same procedure was performed for all of the events in 2D and 3D sea states, and force impulses of the slamming part of the time series were calculated using the **ImpQP** and the **Comb** methods. The results are shown in Fig. 6 as histograms. The x-axes of the plots were normalized by the wave celerity computed on the nominal peak frequency and the measured H_s at the location of the cylinder. In the left plot, the force impulses from the 2D sea states are shown and both the results from the **ImpQP** and the **Comb** method show a skewed distribution with a peak around 0.2 and 0.4 and an extended tail towards larger values. The force impulses from the **ImpQP** method show a wider distribution around the peak. Therefore the results from the **ImpQP** method have a larger number of larger values of force impulse.

In the right plot, similar results are shown for the 3D sea states. The peak value of the histogram distributions is around 0.4 from the **Comb** method results and slightly lower from the **ImpQP** results. The distribution is narrower around the peak for the **Comb** method. In general, this figure shows that the range of the force impulses for the 2D and the 3D cases are very similar. Further, the mean of the 2D impulses is smaller than for the 3D impulses. This will be quantified in Section 4.5. We note, though, that this is based on a relatively small number of 2D events (117), relative to the larger number of 3D events (487).

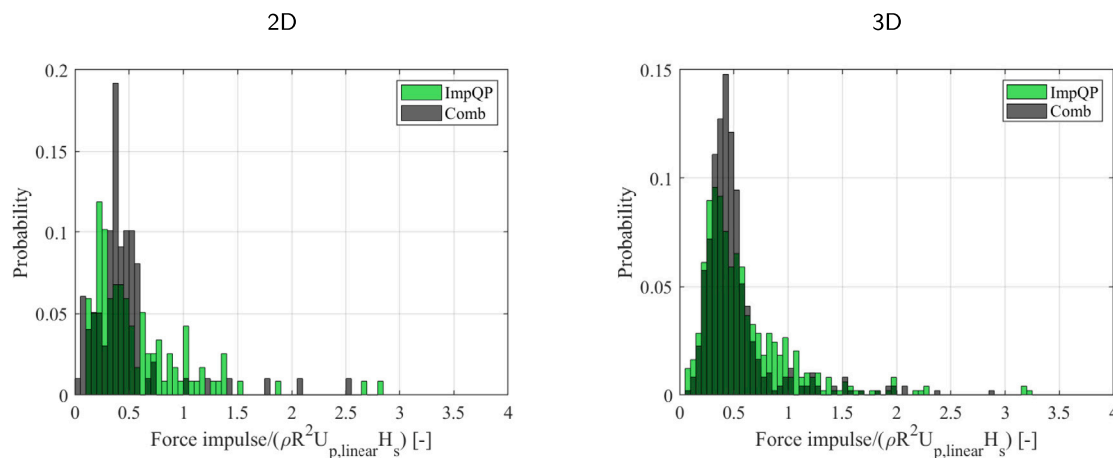


Fig. 6. Histograms of the force impulses calculated from the measurements for 2D (left) and 3D (right) sea states using the **ImpQP** and the **Comb** methods.

The similarities between the results from the **ImpQP** method and the **Comb** indicate that the results are largely reliable. Yet, the differences illustrate the uncertainties in the analysis, where there are no ‘true’ results for the slamming loads. The aim for the following validation of the pressure impulse model with fully nonlinear wave kinematics is thus to reproduce the observed impulse statistics within the uncertainty illuminated by the difference of the two extraction methods.

3.4. The difference between the inline and total force impulse

It is worth mentioning that the slamming wave forces in the 3D sea states impose forces with some angle relative to the x -axis. We expect the total force impulses to be larger than their projection on the x -axis. Thus to compare the total force impulses and the force impulses in the x -direction, both were calculated using the **ImpQP**, the **VMD** and the **AggFil** methods. The results are provided in Fig. 7 where it is shown that the difference between the total force impulses (in grey) and the force impulses in the x -direction (in red) is small in two of the three methods. In Figs. 7(a) and 7(c), using the **ImpQP** and **AggFil** methods respectively, the x -direction force impulses are only marginally smaller than the total force impulses, while in Fig. 7(b) the total force impulses are in some cases twice as large as the x -direction force impulses.

The differences between these results partly originate in the fact that the y -component of the force time series has different dominant frequencies than the ones in the x -direction. This difference is because the y -component of the force has both contributions from the wave loads with some relatively small angle from the x -axis and the lift forces imposed on the cylinder from the waves which is mostly in the y -direction. Since the two contributions are comparable in magnitude and frequency, separating the non-slamming part from the total force is more difficult than in the x -direction.

Because of this difference in the frequency content of the forces in the y -direction, the methods explained in the previous section are also less successful in isolating the non-slamming part of the signal and the results in the other cases are not as reliable as for the x -direction. In the **ImpQP** method, the first step is to search for the turning point and then search for a point proceeding to the peak of the time series where the slope of the fit is closer than 10% to the original time series. Adding the y -component of the force time series, which has higher frequencies can change the first and the second intersections of the non-slamming and slamming force time series. The **VMD** method is influenced more by the addition of the y -component of the force since it separates a different set of intrinsic modes. Hence, choosing the fifth mode does no longer correspond to the slamming part of the signal. This large difference is evident in Fig. 7(b). Similarly, the addition of the y -component forces contaminates the separated slamming force impulses

using the **AggFil** method. However, the **AggFil** method is most robust against the contamination of the total force by the forces in the y -direction. Since the **StExpF** and **StExp η** methods rely on linearizing the scalar time series of free surface elevation and inline force, they cannot be applied to the forces in the y -direction in their present formulation.

Because of the mentioned difficulties in the separation of the slamming forces in the y -direction and the small contributions shown in Figs. 7(a) and 7(c), the slamming force impulses and time series were only calculated in the x -direction after this.

4. Calculation of force impulses from 2D and 3D wave kinematics

In this section, we describe the details of the two numerical models used to reproduce the experimental slamming wave loads, namely the potential flow solver OceanWave3D (Engsig-Karup et al., 2009) and the PIMP model (Ghadirian and Bredmose, 2019b). The OceanWave3D computations, which were run on DTU Computing Center (2021)’s computational resources, were conducted by Pierella et al. (2021b) and reused here. In addition, the methods for choosing the possible slamming events in the reproduced waves and using the wave characteristics as inputs to the PIMP model are also explained. The statistics of the model calculated force impulses are compared against the measurement results at the end of this section.

4.1. Computational domain for the wave kinematics

The 2D simulations were made on a grid with a length of 1300[m] full scale. The domain for the 2D computations had $(N_x, N_z) = (513, 17)$ points, while the 1000[m] wide 3D domain was discretized with $(N_x, N_y, N_z) = (257, 37, 15)$ points. The lower resolution in the x -direction was needed to limit the total computational time. The waves were generated in a relaxation zone that was 350.0[m] long. In this zone, several linear realizations of the sea states in Table 1 were input. The phases of the spectrum were generated by random sampling of a uniform distribution with bounds $[0, 2\pi)$. Therefore, we performed a statistical comparison of the waves and associated loads, rather than a deterministic one.

The waves were absorbed in a 350.0[m] long absorption zone positioned at the end of the computational domain. On the sides of the 3D domain, two further absorption zones were located, with a width of 100.0[m] each, to absorb waves travelling in oblique directions.

The formulation of the fully nonlinear potential flow solver does not allow for the direct physical modelling of wave breaking. Instead, a breaking filter is coupled to the solver, which smooths a three-point region of the free surface elevation and the free surface potential around the points where the downward particle acceleration at the free surface

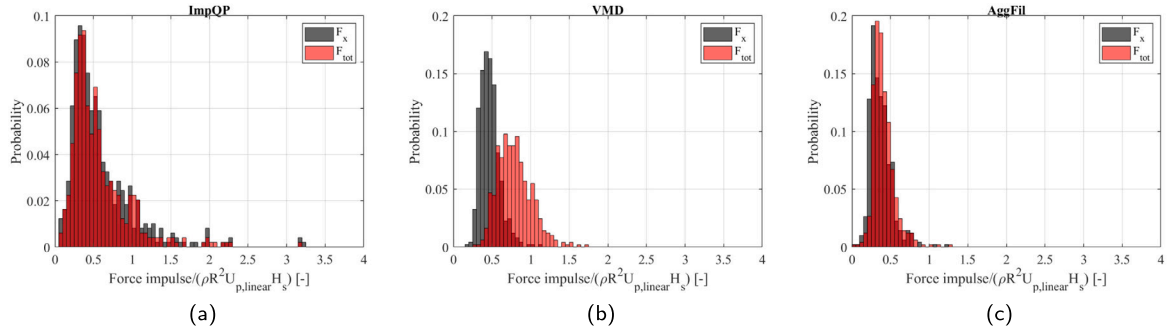


Fig. 7. The total and x-direction slamming force impulses calculated from the measurements using the three methods of ImpQP, VMD and AggFil.

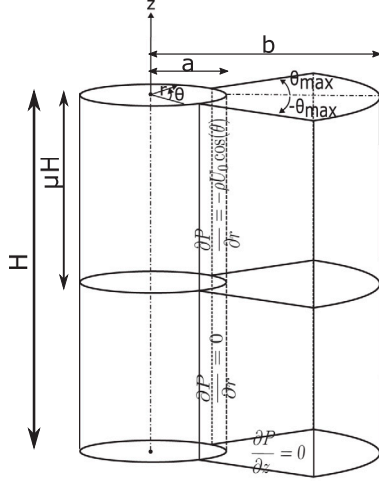


Fig. 8. The wedge-shaped 3D impact on a vertical circular cylinder for which the Pressure Impulse model is solved (Ghadirian and Bredmose, 2019b).

overcomes a threshold of βg , where $g = 9.81[\text{m/s}^2]$ is the gravitational acceleration (Longuet-Higgins, 1969). This subtracts energy from the flow, representing the breaking dissipation, and allows the simulations to remain stable. In the current OceanWave3D computations $\beta = 0.5$ was used, as calibrated by Pierella et al. (2021b).

4.2. The pressure impulse load model

The PIMP model was developed by Ghadirian and Bredmose (2019b) with inspiration from Cooker and Peregrine (1995). It was validated against measurements in Ghadirian and Bredmose (2019a) and CFD computations in Ghadirian and Bredmose (2020a). The pressure impulse is defined as the time integral of the fluid pressure over the duration of the impact

$$P = \int_{t_{\text{before}}}^{t_{\text{after}}} p \, dt \quad (3)$$

Following the derivation of Cooker and Peregrine for a 2D wall impact, it can be shown to satisfy the Laplace equation with boundary conditions of $P = 0$ at free surfaces, $\partial P / \partial n = 0$ at contact with solid boundaries and $\partial P / \partial n = -\rho U_n$ in the impact zone, where U_n is the impact velocity normal to the structural surface.

The PIMP model is formulated for a wedge-shaped domain of height H adjacent to a vertical cylinder and solved through separation of variables and Fourier analysis. A drawing of the domain is shown in Fig. 8. The boundary conditions of the problem are also shown in Fig. 8.

The solution was given by Ghadirian and Bredmose (2019b) as

$$P = \sum_{m=1}^{\infty} \sum_{n=1}^{\infty} \left(A_{mn} \cos(L_m \theta / \theta_{\max}) \sin(k_n \frac{z}{H}) \right)$$

$$\times \frac{I_{q_m}(k_n \frac{r}{H}) + \alpha_{mn} K_{q_m}(k_n \frac{r}{H})}{\partial_r \left(I_{q_m}(k_n \frac{r}{H}) + \alpha_{mn} K_{q_m}(k_n \frac{r}{H}) \right)_{r=a}}, \quad (4)$$

where $L_m = (m - 1/2)\pi$, $k_n = (n - 1/2)\pi$ and $q_m = L_m / \theta_{\max}$ is the order of the Bessel functions. Further α_{mn} is chosen such that $P = 0$ at $r = b$,

$$\alpha_{mn} = \frac{-I_{q_m}(k_n b / H)}{K_{q_m}(k_n b / H)}, \quad (5)$$

and

$$A_{mn} = \frac{2\rho U}{\theta_{\max}} \frac{1 - \cos(k_n \mu)}{k_n} \int_{-\theta_{\max}}^{\theta_{\max}} \cos(\theta) \cos(L_m \theta / \theta_{\max}) d\theta dz. \quad (6)$$

The non-dimensional pressure impulse thus depends on the relative outer radius of the impacting fluid b/H , the relative height of the impact region μ , the ratio of the inner to outer radius a/b and the maximum impact angle, θ_{\max} .

$$\frac{P}{\rho U H} \left(\frac{r}{H}, \theta, \frac{z}{H} \right) = f \left(\frac{b}{H}, \mu, \frac{a}{b}, \theta_{\max} \right) \quad (7)$$

4.3. Selection of the slamming events in the numerical model

The first step in reproducing the slamming wave force impulses was to identify the waves in the OceanWave3D computations which should be used as the slamming waves. Even though the breaking filter implemented in OceanWave3D helps to extract the excessive energy out of the waves, it was observed that in the current computations it did not result in the same slamming wave frequencies as observed in the experiments at the cylinder location. Hence, since we have determined the frequency of the slamming waves from the measurements in each sea state, the proportionate number of waves with the largest downward vertical accelerations at the free surface was chosen from the OceanWave3D computations. For the general cases, where experimental data of the same sea states are not available, the slamming frequency can be estimated from other works in the literature (see e.g. Dawson et al. (1993), Babanin (2011) and Paulsen et al. (2018)).

Fig. 9 shows the frequency of slamming for each physical test, determined with the methods outlined in Section 3. The mean number of events per hour is shown with a cross, while the error bars show the standard deviation of the number of events between different hours of the tests. The 3D sea states are marked with a green background. By the comparison with Table 1 it is possible to observe that the steepest sea states have a larger number of slamming waves, as expected. Moreover, the frequency of the slamming waves is higher in the 2D sea states than in the 3D cases. This difference is more visible for the sea states with a larger steepness, for example tests 8 (3D) and 13 (2D), while it seems lower for sea states 5 (3D) and 10 (2D), or 19 (3D) and 25(2D).

The effect of the spreading can be seen by the comparison of test 1 (2D), 2 (3D, small spreading) and 3 (3D, large spreading). While the breaking intensity is almost the same for tests 1 and 2, it decreases significantly when a larger spread is used. This may be linked with the

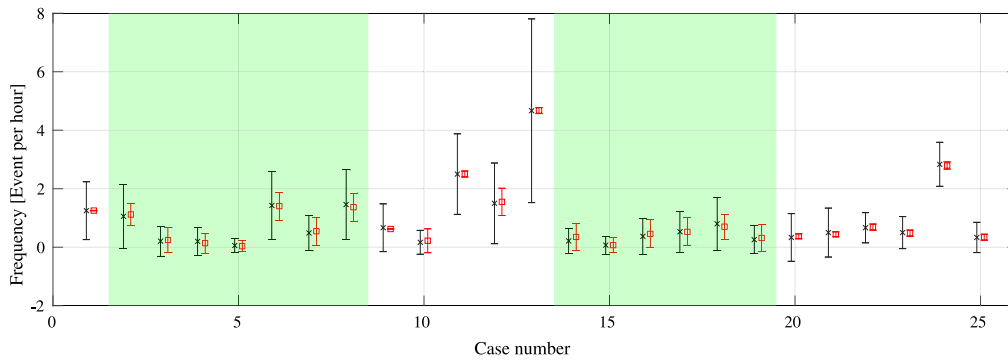


Fig. 9. The slamming frequency of the measurements (in black) and the number of slamming events selected from the OceanWave3D computations (in red). The 3D sea states are marked with a green background.

increased importance of the directional focusing over dispersion focusing as the spreading of the sea state increases, which, as mentioned in Section 2.2.

The experimental slamming frequencies were next used to select the numerical slamming events. Using the average of the measurement slamming frequencies, we first sorted the simulated events by decreasing magnitude of the downward vertical acceleration at the free surface. In the figure, the slamming frequency from the simulations is marked with red markers. In the case of the 3D simulations, the length of the numerical computations was about 1 h each so either one or no slamming event was chosen from these simulations with the probability adjusted to reflect the slamming frequency. It should be noted that the length of the numerical reproductions was different from the corresponding experiments. There were 343 h of simulations for the 2D sea states and 340 h for the 3D sea states. Using the same probability of slamming from each sea state as calculated from the measurements, we ended up with 429 slamming events in the 2D simulations and about 141 in the 3D ones. For 22 out of the 25 sea states, the numerical variation of the slamming frequency (red bar) is smaller than the experimental one (black bars). This suggests that although the experimental and numerical slamming rates have been brought to match, there is still more variability in the hourly slamming rate in the experiments than in the simulations. An improved numerical determination of the slamming rate is left for future work.

4.4. Extraction of the pressure impulse model inputs

After identifying the potentially slamming waves from the OceanWave3D computations, the inputs to the Pressure Impulse model were obtained from the numerical wave kinematics. Several variants of this procedure was tested, with a common aim of a robust and straight forward method. We present here the final procedure and comparison to the extracted experimental force impulses. The azimuth extent of the wedge-shaped water column was $\theta_{max} = \pi/4$, which is based on the previous validations of the model (Ghadirian and Bredmose, 2019b). The total height of the water column was selected as

$$H = h + \eta_{max} \quad (8)$$

where h was the water depth and η_{max} was the maximum free surface elevation of the potentially slamming wave measured from the still water level. The ratio between the slamming part of the water column to the total height was therefore

$$\mu = \frac{\eta_{max}}{\eta_{max} + h}, \quad (9)$$

The outer diameter of the wedge-shaped water column was selected as

$$b = L_p, \quad (10)$$

where L_p was the wave length of the peak period wave calculated using the linear dispersion relation. The velocity of the wavefront was computed as

$$U = \frac{\partial n}{\partial t} = \frac{\eta_t}{\eta_n} = \frac{\eta_t}{\eta_y \sin(\phi) + \eta_x \cos(\phi)}, \quad (11)$$

where n is the axis normal to the wave front at the instant when $|\nabla\eta|$ peaked during the period of the wave, while the wave direction ϕ was computed at the same instant via

$$\phi = \text{atan}(\eta_y/\eta_x). \quad (12)$$

4.5. Force impulse statistics; experiments vs. numerical model

We now compare the force impulses that we calculated from the measurements against the ones calculated using the PIMP model with inputs from the computed nonlinear kinematics. We present the results from both the **Comb** and the **ImpQP** method.

In Fig. 10, the force impulses from the measurements are shown in a grey shaded histogram for 2D, on the left, and 3D sea states, on the right, using the **Comb** method. The y-axis of the plots shows the number of events for each bin of force impulse divided by the total number of events. The most probable force impulse value from the measurements, both 2D and 3D, is of magnitude 0.4, with the tail value extending to 2.0. The 2D impulse histogram seems less converged, as fewer slamming events were sampled in the 2D sea state due to the shorter length of the experiments. In the same figure, the force impulses calculated using the PIMP model are also shown with red bars.

We quantify the match between the distributions in Table 3. Due to the heavy tails of the measured distributions, we included the median values in the table, and will use these instead of the mean values for the discussion. First, for the experimental data, the 2D impulse medians are 10% smaller than for the 3D impulses for both the **ImpQP** and **Comb** analysis. This may be linked to the observed larger frequency of slamming, which was linked to the longer time scale of dispersive wave focusing in 2D which may lead to a weaker local impact violence. Relative to the **Comb** data, the numerical results under-predict the 2D median impulse by about 16% and over-predict the 3D median by 13%. The numerical method thus exaggerates the measured tendency of larger 3D impulses.

We also observe that the distributions of the force impulses from the OceanWave3D-PIMP results are narrower than the experimental ones. This is also visible in Table 3, where the standard deviation of the simulated impulses is about 1/3 of the one from the **Comb** method. Moreover, the tails of the histograms do not extend to the very large force impulse values observed in the experiments. This is reflected in the kurtosis of the simulation results in Table 3, which are about 1/5 of the kurtosis of the experimental force impulses. The smaller variability of the force impulse predicted by the model may be a consequence of our use of a deterministic model (PIMP) for computing the force

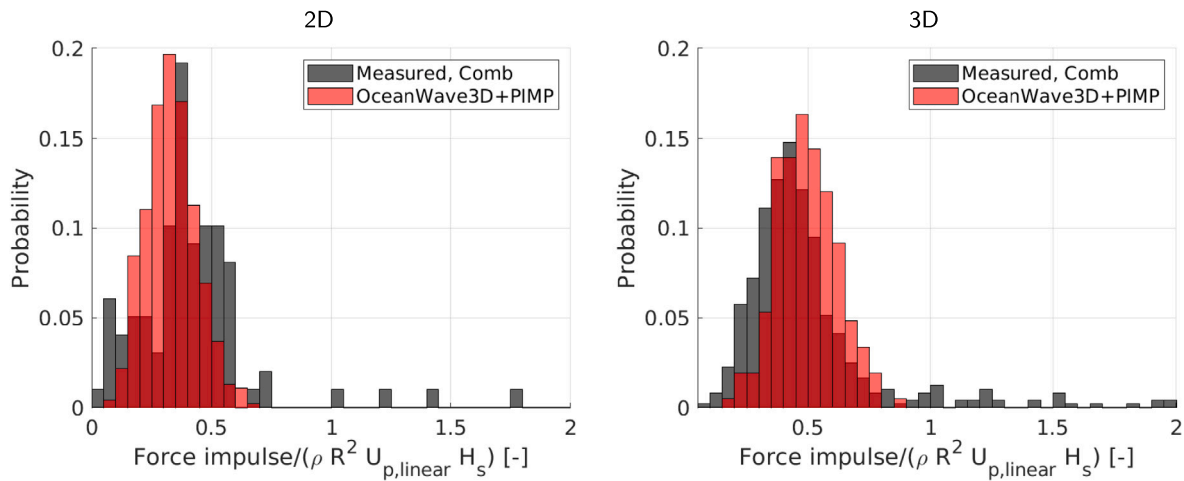


Fig. 10. The force impulse histograms of the slamming events from the measurements and the PIMP-OceanWave3D results for 2D (left) and 3D (right) sea states. The measured force impulses are calculated using the **Comb** method.

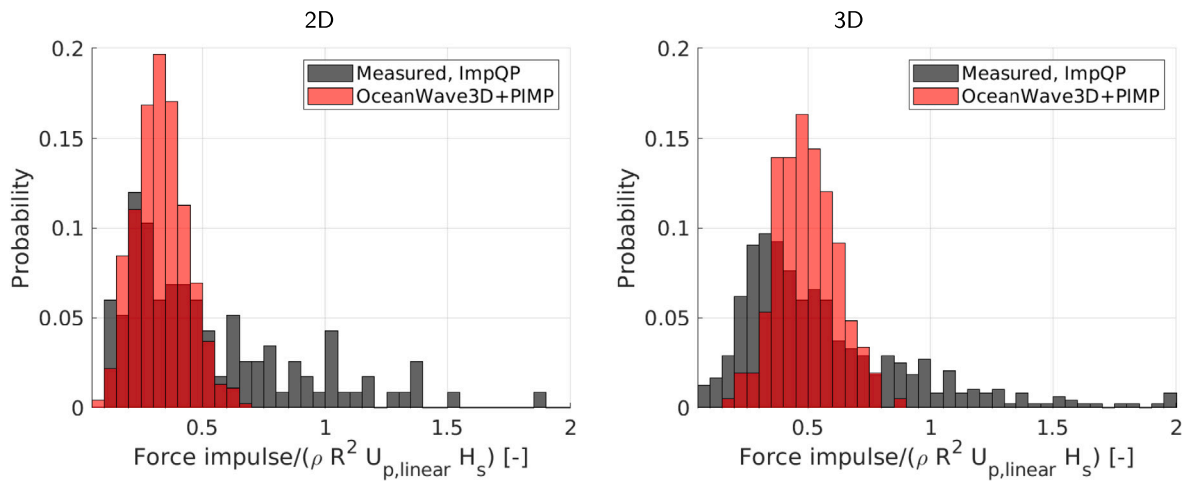


Fig. 11. The force impulse histograms of the slamming events from the measurements and the PIMP-OceanWave3D results for 2D (left) and 3D (right) sea states. The measured force impulses are calculated using the **ImpQP** method.

Table 3
Estimated parameters of the force impulse distributions from models and experiments.

Type		Spread	Mean	Median	St.dev.	Skewness	Kurtosis
Exp	ImpQP	2D	0.569	0.427	0.459	2.305	10.34
		3D	0.596	0.476	0.433	2.459	12.01
	Comb	2D	0.454	0.392	0.369	3.309	16.47
3D		0.508	0.432	0.328	3.137	15.90	
Sim	2D	0.333	0.330	0.104	0.286	2.93	
	3D	0.494	0.486	0.121	0.203	2.93	

impulse. In reality, a small change in the shape of a wave could lead to significantly different breaking patterns and therefore different slamming loads. In the numerical flow model, these fine details are not modelled. Here, the spread in the impulse distribution comes from the variability in the time history of the incident wave alone.

Impulse histograms for the **ImpQP** method are shown in Fig. 11. Compared to the results from the **Comb** method, the distributions of the force impulses are wider and predict a higher median values than for the **Comb** method. Thus relative to the **ImpQP** analysis, the numerical force impulse medians are 23% under-predicted in 2D and 2% over-predicted in 3D.

The larger force impulses of the **ImpQP** method can be linked to its numerical procedure which performs a smoother cut of the force peak.

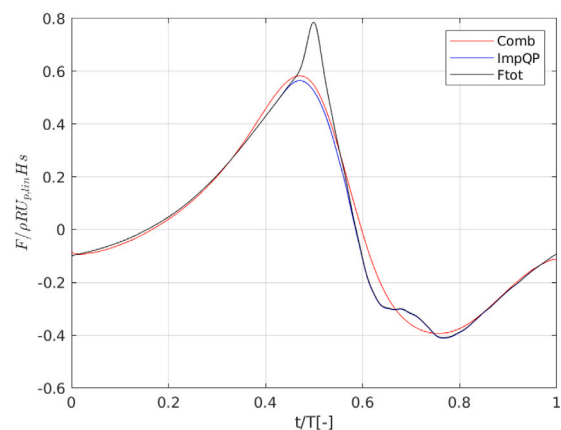


Fig. 12. Average impact time history from the experimental 3D events.

This is illustrated in Fig. 12, where we plot the average of all of the 3D impacts for the two extraction methods. In blue, the **ImpQP** method predicts on average a larger force impulse than the **Comb**.

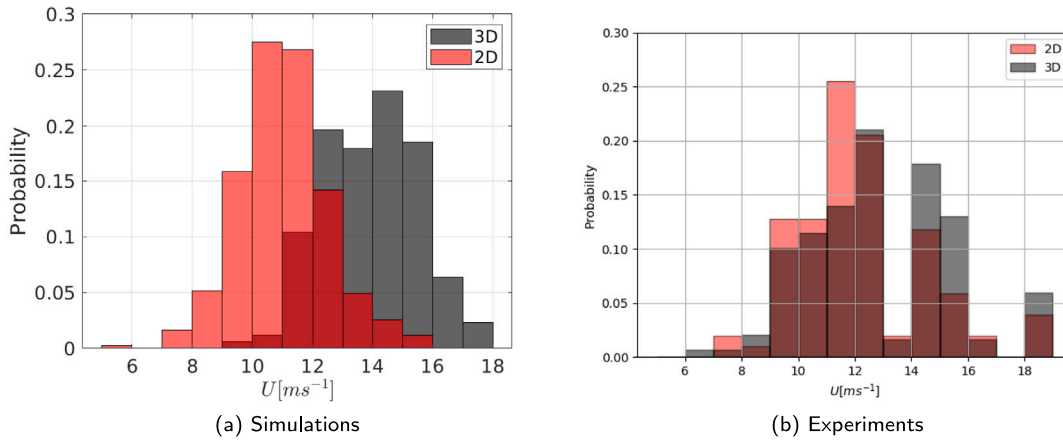


Fig. 13. The wave speed of the 2D and 3D slamming waves from the numerical computations and from the experiments.

From the statistics of the distributions of Table 3, the 2D median impulses are again smaller than for 3D. The higher order statistics of the sampled values are quite in line between the 2D and 3D simulations, except for the kurtosis which is 20% higher for the 3D results.

Overall, from the analysis of Figs. 10, 11 and Table 3, the proposed method for the calculation of the force impulses provides a sound reproduction of the experimental results. Although a closer match to the experimental results is desirable, the difference between the **ImpQP** and **Comb** results illustrates the level of uncertainty and the appropriate level of accuracy. We note that no particular calibration of the numerical model has been carried out. This is possible, in future use, if a certain reference data set is to be matched.

4.6. The difference between 2D and 3D impulses

The numerical results exaggerated the experimental tendency of larger force impulses for 3D sea states. After thorough investigations, it was observed that the large difference in the simulated impulses originates in differences in the final wave front velocities at the location of the cylinder. This is demonstrated in Fig. 13, where the histogram of 2D front velocities peaks at about 10 m/s, and the 3D histogram has a peak at about 14 m/s.

We can now compare the numerical impact velocities with the measured ones. To measure the impact velocity in the experiments, we used the free surface elevation signals from two wave gauges positioned 10 [m] apart in the main wave direction. To obtain the impact velocity for each breaking wave, we extract the time of travel of the wave crest from one wave gauge to the other. In Fig. 13(b), the distribution of the measured impact velocity shows a larger degree of similarity between the 2D and 3D impact velocities, which can explain the closer similarity in the mean values of the 2D and 3D experimental force impulses.

Given the numerical over-prediction of the 3D impulses, it is desirable to calibrate the method to obtain a better match. While further analysis into the observed differences in front velocity is desirable, a straight forward adjustment of the impulse size can be achieved by reducing θ_{max} . Hence, the force impulses in 3D cases were also calculated using $\theta_{max} = \pi/4.5$ and the results are shown in the appendix in Fig. 19. By choosing a smaller θ_{max} the agreement between the model results and the measurements improves. However, because the choice of θ_{max} is expected to be spreading dependent and for the sake of consistency with the 2D cases we chose to use $\theta_{max} = \pi/4$ for all of the cases hereafter.

5. Prediction of the force peaks and time series

In this section, the methodology for extending the model Force Impulse results to slamming load time series is presented. While the force impulse and pressure impulses are based on physical conservation laws, a prediction of the detailed time history requires further assumptions. We here attempt to use a pre-defined time variation which has the right force impulse and can be fitted to match the average shape of the slamming force histories.

To this end, a theoretical investigation of the effect of the height of the overturning wave on the peak force value is introduced. Finally, the slamming load time series, the statistical distribution and the joint probability distribution of the peak force values and the periods are validated against the results from the measurements analysed by the **ImpQP** and **Comb** methods.

5.1. Calculating the slamming force time series

A natural next step after calculating the force impulses from the calculated nonlinear wave kinematics is to provide designers with time series which can be used in the design process. Previously, Paulsen et al. (2018), based on ensemble averaging the experimental time series of slamming wave forces, suggested the following harmonic function:

$$f(t) = \sin^2\left(\frac{\pi t}{\tau}\right), \quad \text{where } t \in \left[0; \frac{13 D}{32 V}\right] \quad (13)$$

where t indicates time, D is the cylinder diameter, V the impact velocity and $\tau = DV_0^{13}/(32)$ was the duration of slamming. A similar approach was taken in the current paper and based on visual inspection of the extracted slamming force series, a similar harmonic function, although in third order, was devised as

$$h(t) = \frac{\cos\left(\frac{t}{\tau/2} \frac{\pi}{2}\right)^3}{\int_{-\tau/2}^{\tau/2} \cos\left(\frac{t}{\tau/2} \frac{\pi}{2}\right)^3 dt} = \frac{3\pi}{4\tau} \cos\left(\frac{t}{\tau/2} \frac{\pi}{2}\right)^3 \quad -\tau/2 \leq t \leq \tau/2, \quad (14)$$

where t indicates time and τ is the unknown slamming duration. Since the integral denominator in Eq. (14) ensures that the integral of this time series remains one, multiplying this equation by the force impulses from the PIMP model results in the slamming force time series

$$F_s(t) = h(t) \int_{-H}^0 \int_{-\theta_{max}}^{\theta_{max}} P\left(\frac{R}{H}, \theta, \frac{z}{H}\right) \cos(\theta) R d\theta dz, \quad (15)$$

where P is the pressure impulse calculated using the PIMP model, i.e. Eq. (7). The same principle can be applied to yield the local pressure time series from the local pressure impulse, by omitting the spatial integration in Eq. (15). The difference between our suggested formulation for the slamming force time series with the one from Paulsen et al.

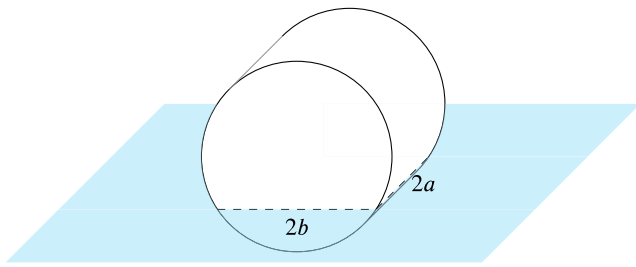


Fig. 14. A drawing of a limited length cylinder entering the water with a cross-section that is $2a$ long and $2b$ wide.

(2018) is conservation of the force impulse in our model, while no assumption is made about the values of the peak line force and the period of slamming.

The slamming period τ in Eq. (15) can be determined from knowledge of the maximum slamming force, F_{\max} . This yields

$$\tau = \frac{3\pi \int_{-H}^0 \int_{-\theta_{\max}}^{\theta_{\max}} P\left(\frac{R}{H}, \theta, \frac{z}{H}\right) \cos(\theta) R d\theta dz}{4F_{\max}} \quad (16)$$

The theoretical peak line force (force per length) of a 2D cylinder entering a flat water surface was calculated by von Karman (1929) and later by Goda et al. (1966) resulting in

$$f_l = C_s \rho R V^2 \quad , \quad C_s = \pi \quad (17)$$

where C_s is commonly referred to as slamming coefficient. The von Karman theory, does not take into account that the water displaced by the cylinder piles up around its sides. Wagner (1932) included this effect in his calculations to obtain $C_s = 2\pi$. A first guess for F_{\max} would therefore be $2\pi \rho R \mu H V_0^2$. This value, however, is far too large, due to the limited length of the impact zone along the cylinder height.

To compare the effect of a 2D cylinder entering the water versus a 3D cylinder with a limited length, we extended the formulation of von Karman (1929). A drawing of a limited length cylinder entering water is shown in Fig. 14. In von Karman's theory, the added mass for the cylinder entry is taken as the added mass of a rectangular plate of width $2b$ and infinite length. We replace this by the added mass c_m for a finite rectangular plate of length $2a$, still with a width of $2b$ (e.g. Sumer et al., 2006). The peak force was calculated for different ratios of a to b for a long cylinder when $a > b$

$$F_{\max} = C_m \pi \rho R V_0^2, \quad (18)$$

and for a short cylinder when $b > a$

$$F_{\max} = C_m \frac{b}{a} \pi \rho R V_0^2. \quad (19)$$

Dividing the peak force by $\rho R V_0^2$ the modified von Karman slamming coefficient for a finite length cylinder is plotted in Fig. 15. For longer cylinders ($a/b > 10$), the slamming coefficient converges to the 2D result $C_s = \pi$, while a significant drop occur for $a < b$.

A value of $C_s = \pi$ (von Karman) or 2π (Wagner) is therefore unrealistically large for slamming wave impacts, where $a < b$. This is also reflected in the work of Wienke and Oumeraci (2005). Although they used a value of $C_s = 2\pi$, their final maximum force was formulated as

$$F_{\max} = \max_x \int f_l dz = \lambda \eta_b C_s \rho R V_0^2 \quad (20)$$

where λ , the curling factor, was tuned by match to experiments of focused wave groups. Here, further, η_b is the surface elevation of the slamming wave. Calibration to a smaller effective slamming coefficient was also carried out by Paulsen et al. (2018), who used a hypothetical, although intuitive, force distribution on the surface of the cylinder for

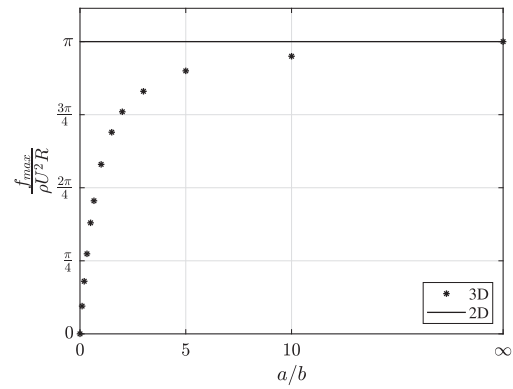


Fig. 15. The slamming coefficient as a function of a/b ratio. The results for a limited length cylinder are shown with black asterisks and denoted 3D while the result of an infinitely long cylinder is shown as a solid red line and denoted 2D.

irregular waves on a sloped bed. This distribution ultimately resulted in

$$F_{\max} = \lambda H_b \frac{2}{\pi^2} 2\pi \rho R V_0^2, \quad (21)$$

where $\frac{2}{\pi^2}$ is the extra multiplicand resulted from the predefined force distribution assumption.

With this insight, we choose in the current work to formulate the maximum inline force as

$$F_{\max} = C_s \rho (U \cos(\phi))^2 R \eta_b \lambda_b \quad (22)$$

with the corresponding period of

$$\tau = \frac{3\pi \int_{-H}^0 \int_{-\theta_{\max}}^{\theta_{\max}} P(z, \theta) \cos(\theta) R d\theta dz}{4C_s \rho (U \cos(\phi))^2 R \eta_b \lambda_b}, \quad (23)$$

with $C_s = 2\pi$ and with an empirical adjustment factor of λ_b . Further here, ϕ and U are the instantaneous angle of the wavefront and the x -axis and the instantaneous velocity of the wave front. We denote λ_b , as the effective curling factor. It was chosen such that the statistical distribution of τ and F_{\max} from the model would be most consistent with the period and peak slamming forces from the measurements in 2D and 3D sea states separately. Consequently, the coefficient λ_b takes into account both the length of the overturning part of the wave and the vertical distribution of the line force.

5.2. Calibration of slamming force peak and period

The peak value and period of the slamming force time series were calculated using Eqs. (22) and (23). In Fig. 16, the peak force and period of the slamming forces are shown for the ImpQP analysis for the 2D and 3D sea states along with the model results. In the 2D cases λ_b was calibrated to $0.55/\pi^2$ and in the 3D cases $\lambda_b = 0.4/\pi^2$.

In the 2D results from the measurements, the nondimensional peak force distribution peaks around 0.15 and the nondimensional period distribution peaks around 4 with an unconverted distribution. The tail of the force peak distribution reaches up to 0.8 and τ reaches up to 12. Similarly, for the 3D experimentally based results, the distribution of the peak forces peak at around 0.2 and the periods peak at around 4. The tail of the distribution of the periods extends to 25 for a few events. The difference in the tail of the distributions in the 3D and 2D cases might be because of the larger number of events in the 3D cases.

The force peak distributions from the model results are very close to the measurement results in both 2D and 3D. However, the model results have narrower distributions. The slamming period distribution from the model results, shown in the right-hand side plots by red bars, are also in good agreement with the measurement results. Also for the period

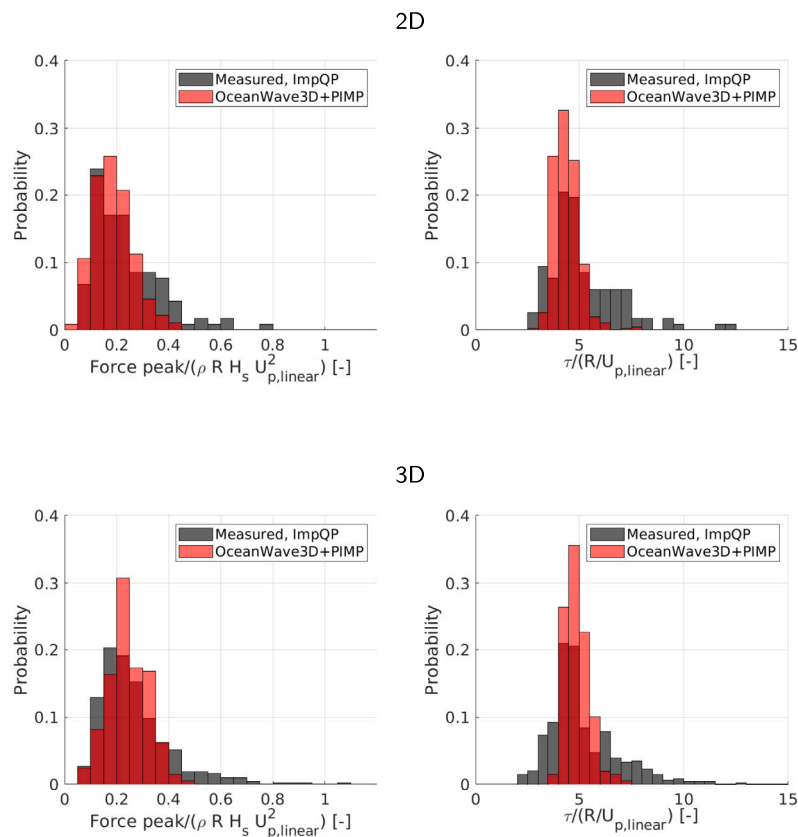


Fig. 16. Histograms of peak force (left) and period (right) of the slamming forces in 2D (top row) and 3D (bottom row) sea states from the measurement and model results. The measurement slamming forces were isolated using the **ImpQP** method.

case, the distributions of the model results have narrower distributions than the results from the measurements.

Our assumption in writing Eq. (22) and (23) implies an inverse proportionality between F_{max} and τ for fixed force impulse. Although Fig. 16 demonstrates that the marginal distributions of force peak and period are well represented with the calibrated model, it is valuable to look at the joint distribution of F_{max} and τ . Hence scatter plots of the slamming period versus the peak values are shown in the top row of plots in Fig. 17 for the 2D and 3D sea states with their joint probability density estimates in the bottom row. Consistently with Fig. 16 the most probable combination within the measurement based results has a force peak of 0.15 and period of 4.5 in 2D and a force peak value of 1.7 and period of 4.5 in 3D, all given in normalized units.

The peak for the joint probability distribution for the 2D numerical results coincides with the measurement based peak. The joint probability distribution of the numerical results, however, is shaped differently than the measurement based distribution and reflects the inverse proportionality between F_{max} and τ . Further, the model result has a narrower distribution in the calculated τ than the results from the measurements as also visible from the marginal distribution in Fig. 16. A similar shape difference occurs for the 3D numerical probability distribution, although with a slightly less pronounced impact from the inverse proportionality of F_{max} and τ . The peak of the distribution, however, is shifted towards a larger force peak value and a larger period value.

We next used Eq. (15) to calculate the averaged slamming force time series from the given force impulses for all the 3D and 2D cases. This was achieved by alignment of the peak instants and subsequent averaging. Similarly, the isolated measured slamming force time series were aligned to their peak time and averaged. The results are shown in Fig. 18. The mean results from the measurements are shown with black solid lines while the one-standard-deviation range around them

is shown in grey for both the 2D and 3D sea states. The averaged model results are also shown in these plots with red curves and their standard deviation with pink shades around them. The averaged model time series resemble the averaged measured slamming force time series, although some asymmetry can be seen in the measurement based results with a slower decline after the force peak. For the 2D results, some under-prediction of the force peak and average impulse is seen, consistent with Table 3. For the 3D results, the mean force peak is matched quite well. Further, for both 2D and 3D, the standard deviation shades are generally wider around the measurement results compared to the model results. This is consistent with the histograms of Fig. 16, where the results from the measurements had wider histograms of peak and period compared to the model results.

Similar to the above analysis based on the **ImpQP** method, the model slamming force time series were also validated against the measurement results from the **Comb** method. The associated histograms, scatter plots, joint probability distributions and averaged force time series are shown in Appendix. For the histograms in Fig. 20, there is generally a good match to the measurements, although with some numerical over-prediction of the 3D periods. The match between the numerical and measurement based joint probability distributions is slightly better than for the **ImpQP** method, although the numerical 3D peak still exceeds the measurement based peak for force and period. For the averaged time series, in Fig. 22, there is a good match for shape and force peaks, although the asymmetry again implies a general under-prediction of the impulse. Although one may thus prefer the **Comb** results, we note that their difference to the **ImpQP** results is due to the analysis method, where no ‘true’ answer exists. The difference thus illustrates the uncertainty related to the separation of the slamming loads from the main wave loads.

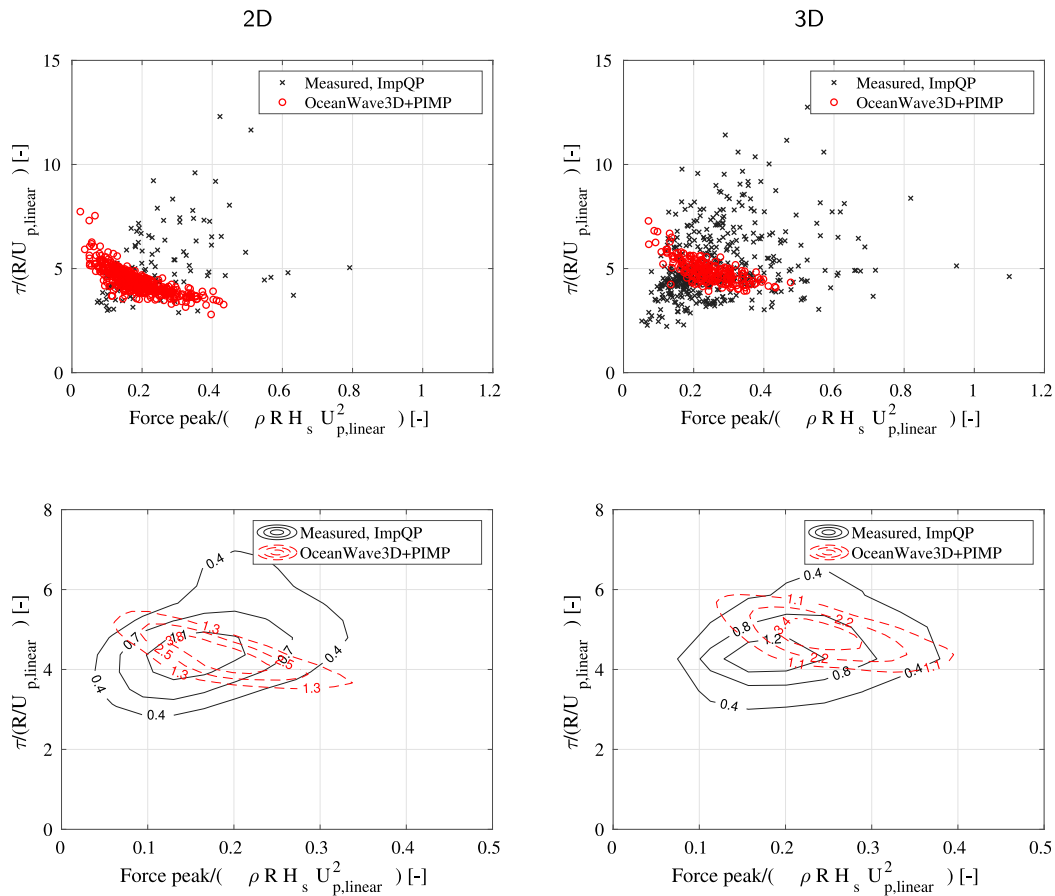


Fig. 17. The scatter plots of the slamming forces period versus the peaks for results from the measurement, using the **ImpQP** method, and the model in 2D, on the left, and 3D sea states, on the right-hand side.

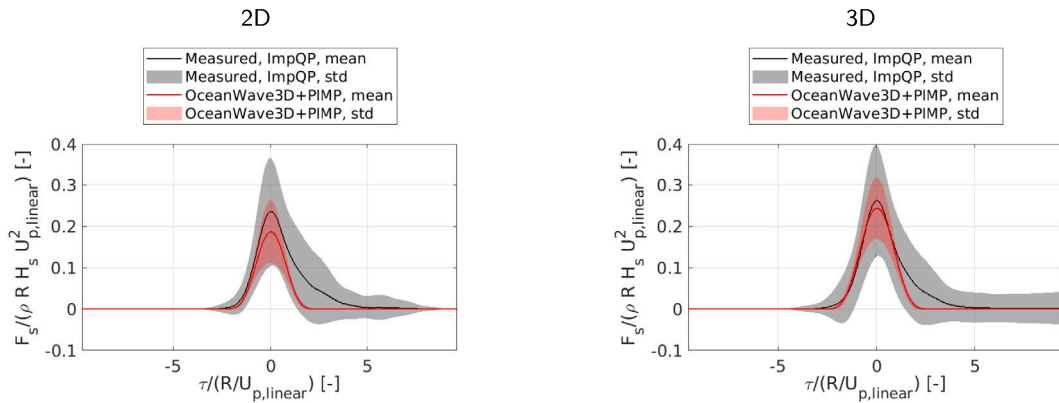


Fig. 18. Slamming force time series from the measurements and the model results in 2D, left, and 3D, right, sea states. The slamming forces from the measurements were isolated using the **ImpQP** method.

6. Incorporation in design

The most important implication of the present results is that the applied methodology can be used to calculate the force impulses with a limited number of assumptions. The main calibration parameter in the Pressure Impulse model is θ_{max} which is set to $\pi/4$. The other parameters of the PIMP model are easily and intuitively obtained from the kinematic outputs of OceanWave3D and it was observed that the

inputs to the PIMP model do not need extra calibration for 2D or 3D sea states.

In addition, a recipe for calculating a slamming force time series based on the model force impulse was proposed which showed a generally good agreement with the measurements. With one assumption for the shape of the time series and the relation between the period and the peak value of the time series, only calibration of the effective curling factor, λ_b , was needed. This parameter was tuned separately for the 2D and 3D sea states.

A direct implementation of this work is its application in the design process. Given a specific sea state, the empirical probability distribution of the peak slamming forces can be calculated from the proposed method and time series of nonlinear wave kinematics. For the latter, an extensive data base is available, as published by Pierella et al. (2021c) within the DeRisk project. The data base covers a wide range of sea states. Slamming calculation can next be repeated for several sea states and an extreme value fit can be used for predicting the extreme peak slamming force with a return period of for example 10,000 years. This is similar to the work by Sørensen et al. (2021) who combined the short term probability distribution of non-slamming force peak values from the DeRisk database with the long term probability of the extreme sea states from Hansen et al. (2020). Using the current work methodology, a similar generalized extreme value probability can be created for the slamming force peak values.

Finally, the results and observations of this paper should be interpreted with consideration for the limitations and uncertainties involved. The first uncertainty in the validation of the model is recognizing the slamming waves on the cylinder. Our investigation only included the waves that impose the largest loads on the cylinder since the slamming waves that do not impose large waves on the structure are unimportant in this context. This choice was made for reducing the investigation time.

There are also uncertainties associated with the isolation of the slamming loads from the total wave loads imposed on the structure. Each of the six methods used in this study for this purpose is based on some assumptions. The most significant one is the assumption that the wave load can be separated into the slamming and non-slamming parts. Next, the difference between the results of the six methods illustrate the uncertainties involved in the slamming load isolation. We also note that our method of calculating the slamming wave load is based on the assumption that the structure does not move while the load is exerted.

7. Conclusions

In this paper, we presented a robust and validated method for applying the pressure impulse model together with nonlinear kinematics of the incident waves. The recipe was validated against 604 slamming events detected from a lab data set equivalent to 954 h of full scale wave loads on a vertical surface piercing cylinder in storm conditions. Six approaches were tested for separating the slamming loads from the non-slamming part of the force time series. It was observed that none of the developed methods was superior to the others in all of the slamming wave events. Therefore, a method (**Comb**) for combining four of the methods based on the residual error was developed and applied along with a method based on a polynomial fit, **ImpQP**. This is, to the best of the authors' knowledge, the most thorough investigation of slamming force isolation to date.

In the slamming events of the sea states with directional spreading, the force impulses were calculated in both the instantaneous wave direction and average wave propagation direction (x). The difference between the resulting distributions of the force impulses was marginal while the application of four of the slamming force isolation methods was challenging in the instantaneous wave direction. Hence, we chose to proceed with calculating and comparing the force impulses in the average wave directions. The error caused by this simplification is assumed to be a function of the directional spreading of the sea state. Further validation for 3D sea states with different spreadings is therefore recommended as future work.

The frequency of slamming in all of the sea states was calculated and it was noticed that the frequency of the slamming events was larger in the 2D sea states than in the 3D sea states with directional spreading. The 3D force impulses, however, were seen to have a larger mean value. This difference was explained by the mechanism that with directional spreading, the same crest height can be created faster as the waves with different frequencies can travel from different directions and meet at

once in the target location, while in a 2D sea state the constituent waves have to pass each other with (sometimes slightly) different phase speeds which is likely to increase the spatial extent of the breaking process and decrease the breaking intensity.

Next, to drive the PIMP model with fully nonlinear kinematics, we selected a proportionate number of the wave episodes from the computations with the largest downwards particle acceleration according to the respective experimental slamming frequencies. Then, based on examination of a variety of schemes, a robust and simple procedure for choosing the input variables from the wave kinematics outputs was presented. In this method, the height of the impact zone is defined as the height of the impacting wave crest measured from the still water level and the impact velocity is based on the numerical celerity of the wave front. In terms of the **Comb** method, the median of the 2D impulses was reproduced with an under-prediction of 16%, while the 3D impulse median was reproduced with a 13% over-prediction. For the **ImpQP** method, the 2D median under-prediction was larger (23%) while the 3D median over-prediction was smaller (2%). The model reproduced the trend of larger 3D impulses than 2D impulses.

The level of agreement for the measured and modelled results verified the applicability of the proposed PIMP model and its application methodology to be used in general situations by designers. Although a better match to the measurement based data is desirable, the difference between the results of the **Comb** and **ImpQP** methods illustrates the level of uncertainty. While the present method is robust and calibration free, further calibration can be applied to match specific data sets or benchmark targets. Also a direct numerical determination of the slamming rate is left for future work.

Given the robust match of the force impulses in both 2D and 3D, we pursued the prediction of the force time history of the individual slamming events. We based this on a fixed bell-shaped (\cos^3) time history which matches the force impulse, and where the force peak value and impact duration are inversely proportional. We were able to achieve a generally good match for the marginal probability distributions of the force peaks and impact duration by defining and calibrating the effective curling factor, λ_b . For the joint probability distribution, however, the proposed method was affected by the choice of a prescribed model time history. Based on the fitted 2D and 3D curling factors, a generally good match for the averaged slamming time series was found, with some under-prediction of the mean force peaks when compared to the **ImpQP** detected slamming events in 2D, but with a good match to those of the **Comb** based analysis.

In the context of the peak values of the slamming force, we found that the classical slamming coefficient of 2π is not realistic. This was explained by the limited vertical extent of the impact zone, which is far from the 2D cylinder impact regime associated with the 2π value. This explains why the curling factor in earlier studies is usually very small compared to the height of the impacting crest. Keeping the value of 2π it was possible to calibrate the effective curling factor in our model, to reach a good match for the peak forces. The values in 2D and 3D were different. This indicates that the value is generally a function of the sea state directional spreading.

The new method for slamming load prediction allows the combination of a physics-based pressure impulse load and stochastic fully nonlinear sea states. In combination with pre-calculated kinematics, it can provide fast and physics-based predictions of the slamming impulse and the expected load histories.

CRedit authorship contribution statement

Amin Ghadirian: Conceptualization, Methodology, Data curation, Software, Validation, Analysis, Visualisation, Writing. **Fabio Pierella:** Computations, Analysis, Visualization, Software, Methodology, Writing – review & editing. **Henrik Bredmose:** Conceptualization, Methodology, Writing – review & editing, Supervision, Project administration, Funding acquisition.

Declaration of competing interest

The authors declare that they have no known competing financial interests or personal relationships that could have appeared to influence the work reported in this paper.

Data availability

Data will be made available on request.

Acknowledgment

This work was funded by the Danish Innovation Fund project De-Risk, grant no. 4106-00038B.

Appendix. Additional results

See Figs. 19–22

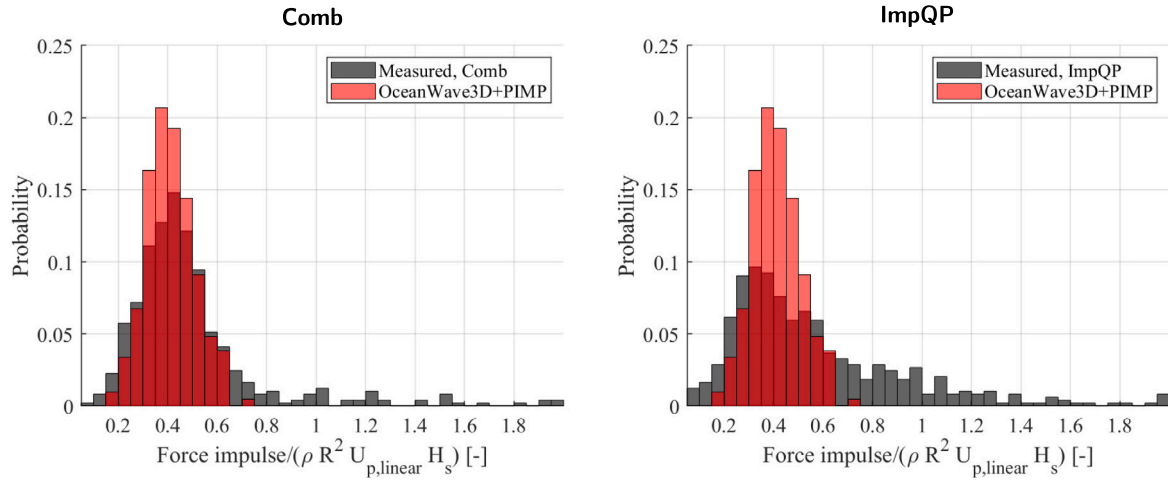


Fig. 19. The force impulse histograms of the slamming events from the measurements and the PIMP-OceanWave3D results. The model results are calculated with $\theta_{max} = \pi/4.5$.

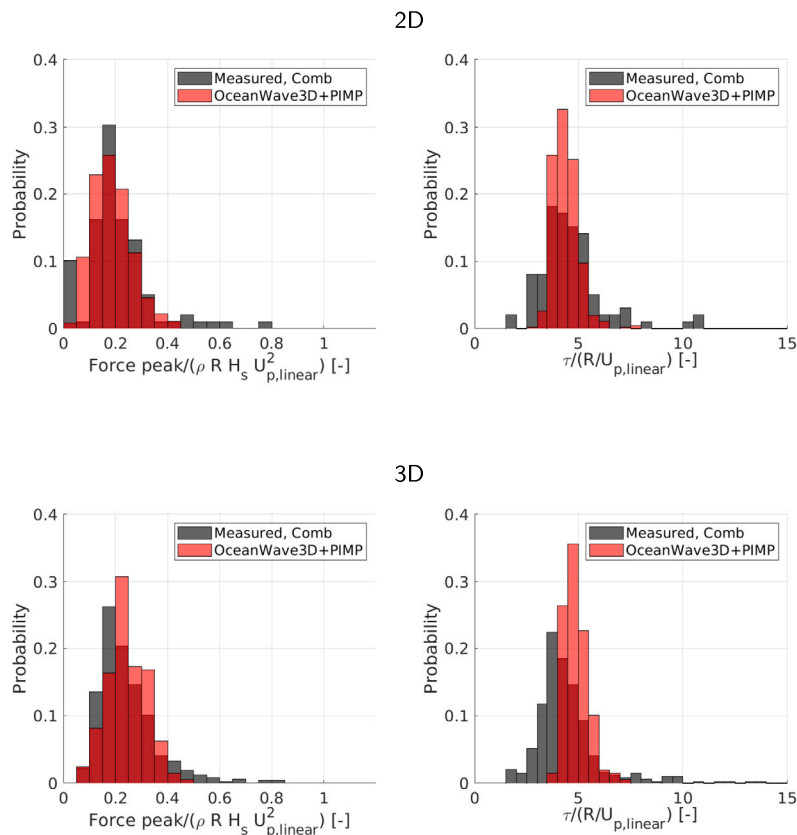


Fig. 20. Histograms of peak force (left) and period (right) of the slamming forces in 2D (top plots) and 3D (bottom plots) sea states from the measurement and model results. The measurement slamming forces were isolated using the Comb method.

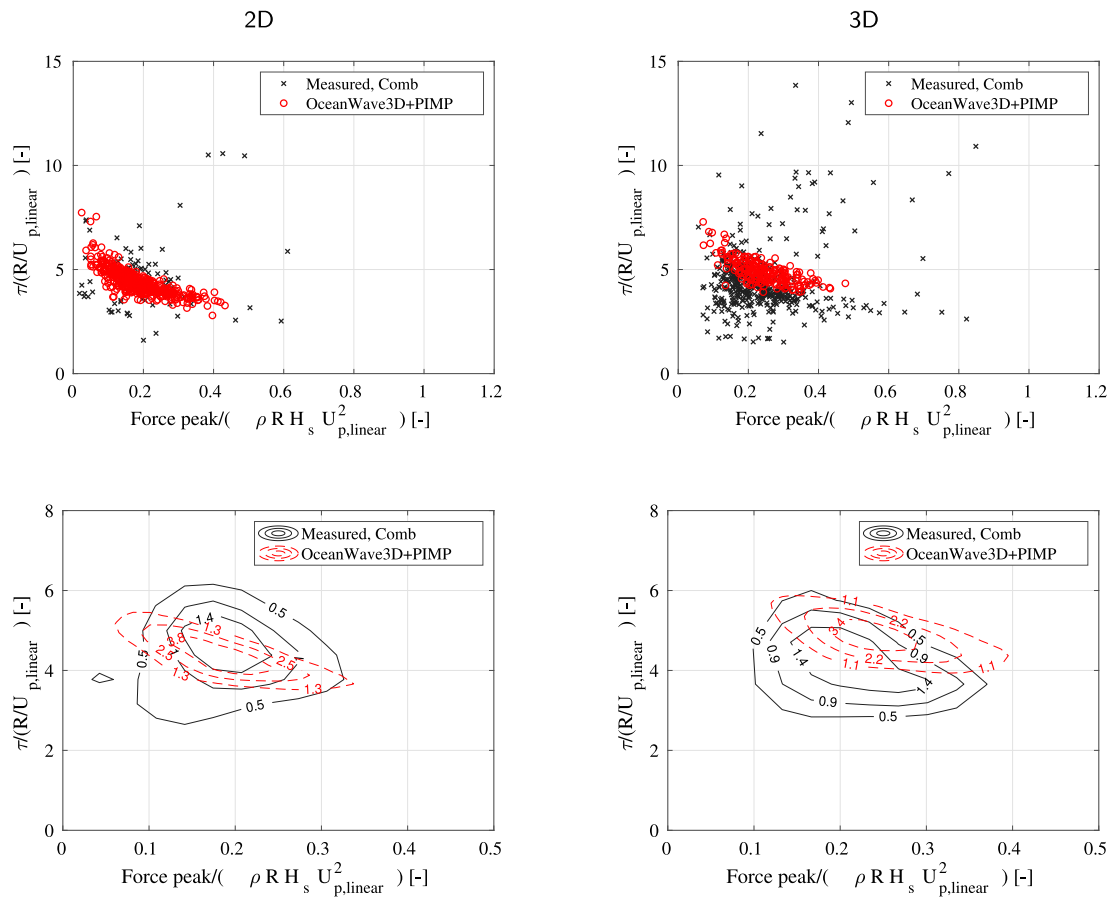


Fig. 21. The scatter plots of the slamming forces period versus the peaks for results from the measurement, using the **Comb** method, and the model in 2D, on the left, and 3D sea states, on the right-hand side.

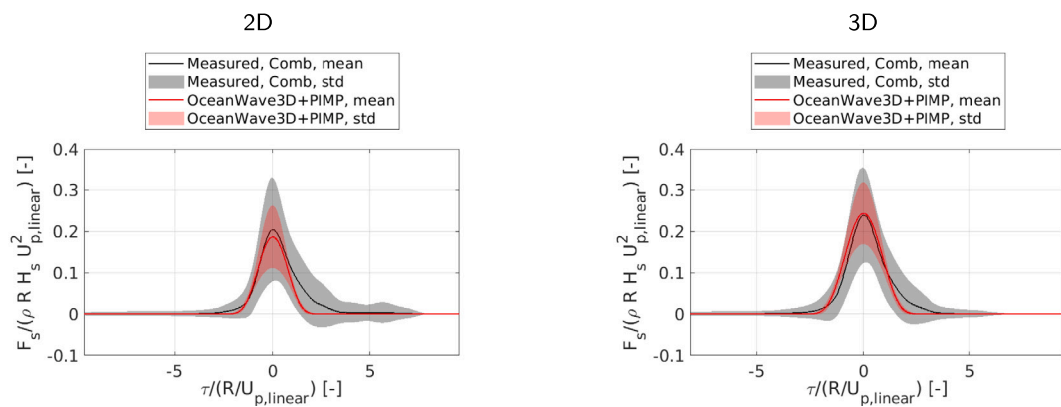


Fig. 22. Slamming force time series from the measurements and the model results in 2D, left, and 3D, right, sea states. The slamming forces from the measurements were isolated using the **Comb** method.

References

- Alsalah, A., Holloway, D., Mousavi, M., Lavroff, J., 2021. Identification of wave impacts and separation of responses using EMD. *Mech. Syst. Signal Process.* 151, 107385. <http://dx.doi.org/10.1016/J.YMSSP.2020.107385>.
- Babanin, A., 2011. *Breaking and Dissipation of Ocean Surface Waves*, first ed. (January 2011), Cambridge University Press, pp. 1–463. <http://dx.doi.org/10.1017/CBO9780511736162>.
- Bredmose, H., Diken, M., Ghadirian, A., Larsen, T., Schløer, S., Andersen, S., Wang, S., Bingham, H., Lindberg, O., Christensen, E., Vested, M., Carstensen, S., Engsig-Karup, A., Petersen, O., Hansen, H., Mariegaard, J., Taylor, P.H., Adcock, T., Obhrai, C., Gudmestad, O., Tarp-Johansen, N., Meyer, C., Krokstad, J., Suja-Thauvin, L., Hanson, T., 2016. Derisk — Accurate prediction of ULS wave loads. Outlook and first results. *Energy Procedia* 94, 379–387. <http://dx.doi.org/10.1016/j.egypro.2016.09.197>, <https://www.sciencedirect.com/science/article/pii/S1876610216308657>, <https://linkinghub.elsevier.com/retrieve/pii/S1876610216308657>.
- Bredmose, H., Jacobsen, N.G., 2010. Breaking wave impacts on offshore wind turbine foundations: Focused wave groups and CFD. In: *Proceedings of the ASME 29th 2010 International Conference on Ocean, Offshore and Arctic Engineering OMAE2010 June 6-11, 2010, Shanghai, China*. pp. 397–404. <http://dx.doi.org/10.1115/OMAEO2010-20368>, [arXiv:https://asmedigitalcollection.asme.org/OMAE/proceedings-pdf/OMAEO2010/49118/397/4587792/397_1.pdf](https://arxiv.org/abs/https://asmedigitalcollection.asme.org/OMAE/proceedings-pdf/OMAEO2010/49118/397/4587792/397_1.pdf).
- Bredmose, H., Jacobsen, N.G., 2011. Vertical wave impacts on offshore wind turbine inspection platforms. In: *Proceedings of the ASME 2011 30th International Conference on Ocean, Offshore and Arctic Engineering OMAE2011. Vol. 5*, pp. 645–654. <http://dx.doi.org/10.1115/OMAEO2011-49785>, [arXiv:https://asmedigitalcollection.asme.org/OMAE/proceedings-pdf/OMAEO2011/44373/645/4594522/645_1.pdf](https://arxiv.org/abs/https://asmedigitalcollection.asme.org/OMAE/proceedings-pdf/OMAEO2011/44373/645/4594522/645_1.pdf).
- Chen, L.F., Zang, J., Taylor, P.H., Sun, L., Morgan, G.C., Grice, J., Orszaghova, J., Ruiz, M.T., 2018. An experimental decomposition of nonlinear forces on a surface-piercing column: Stokes-type expansions of the force harmonics. *J. Fluid Mech.* 848, 42–77. <http://dx.doi.org/10.1017/jfm.2018.339>.
- Cooker, M.J., Peregrine, H., 1995. Pressure-impulse theory for liquid impact problems. *J. Fluid Mech.* 297, 193–214. <http://dx.doi.org/10.1017/S0022112095003053>.
- Dawson, T.H., Kriebel, D.L., Wallendorf, L.A., 1993. Breaking waves in laboratory-generated JONSWAP seas. *Appl. Ocean Res.* 15 (2), 85–93. [http://dx.doi.org/10.1016/0141-1187\(93\)90023-Q](http://dx.doi.org/10.1016/0141-1187(93)90023-Q).
- Dixen, M., 2019. *Work package 2 final report for the DeRisk danish innovation project*. Technical Report, DHI Denmark.
- Dragomireskiy, K., Zosso, D., 2014. Variational mode decomposition. *IEEE Trans. Signal Process.* 62, 531–544. <http://dx.doi.org/10.1109/TSP.2013.2288675>.
- DTU Computing Center, 2021. DTU computing center resources. <http://dx.doi.org/10.48714/DTU.HPC.0001>.
- Engsig-Karup, A.P., Bingham, H.B., Lindberg, O., 2009. An efficient flexible-order model for 3D nonlinear water waves. *J. Comput. Phys.* 228, 2100–2118. <http://dx.doi.org/10.1016/j.jcp.2008.11.028>.
- Fitzgerald, C., Taylor, P.H., Taylor, R.E., Grice, J., Zang, J., 2014. Phase manipulation and the harmonic components of ringing forces on a surface piercing column. *Proc. R. Soc. Lond. Ser. A Math. Phys. Eng. Sci.* 470, 20130847. <http://dx.doi.org/10.1098/rspa.2013.0847>.
- Ghadirian, A., Bredmose, H., 2019a. Initial experimental validation of a pressure impulse model for a vertical circular cylinder. In: *Proceedings of the International Workshop on Water Waves and Floating Bodies (IWWWFB) 2019, Newcastle, Australia*.
- Ghadirian, A., Bredmose, H., 2019b. Pressure impulse theory for a slamming wave on a vertical circular cylinder. *J. Fluid Mech.* 867, R1. <http://dx.doi.org/10.1017/jfm.2019.151>, URL <https://www.cambridge.org/core/product/identifier/S0022112019001514/type/journal-article>.
- Ghadirian, A., Bredmose, H., 2020a. CFD based detection of slamming loads for calibration of a pressure-impulse model. In: *The 35th International Workshop on Water Waves and Floating Bodies (IWWWFB) 2020, Virtual Event*.
- Ghadirian, A., Bredmose, H., 2020b. Detailed force modelling of the secondary load cycle. *J. Fluid Mech.* <http://dx.doi.org/10.1017/jfm.2020.70>.
- Ghadirian, A., Bredmose, H., Schløer, S., Diken, M., 2017. Extreme wave impacts on monopiles: Re-analysis of experimental data by a coupled CFD solver. In: *Volume 1: Offshore Technology. Vol. 1, ASME*, <http://dx.doi.org/10.1115/OMAEO2017-61727>, V001T01A050, URL <http://proceedings.asmedigitalcollection.asme.org/proceeding.aspx?doi=10.1115/OMAEO2017-61727>.
- Ghadirian, A., Vested, M.H., Carstensen, S., Christensen, E.D., Bredmose, H., 2021. Wave-current interaction effects on waves and their loads on a vertical cylinder. *Coast. Eng.* 103832. <http://dx.doi.org/10.1016/j.coastaleng.2020.103832>.
- Godá, Y., 2010. Reanalysis of regular and random breaking wave statistics. *Coast. Eng.* 52, 71–106. <http://dx.doi.org/10.1142/S0578563410002129>.
- Godá, Y., Haranaka, S., Kitahata, M., Godá, Y., Haranaka, S., Kitahata, M., 1966. Study on impulsive breaking wave forces on piles. Technical Report, 6, Port and Harbour Technical Research Institute, pp. 1–30, URL https://www.pari.go.jp/en/report_search/detail.php?id=1966040050601.
- Grue, J., Bjørshol, G., Strand, Ø., Ohkusu, M., 1994. Nonlinear wave loads which may generate ‘ringing’-responses of offshore structures. In: *Ninth International Workshop on Water Waves and Floating Bodies. Vol. 17*, p. 55.
- Gustafsson, F., 1996. Determining the initial states in forward-backward filtering. *IEEE Trans. Signal Process.* 44, 988–992. <http://dx.doi.org/10.1109/78.492552>, URL <http://ieeexplore.ieee.org/document/492552/>.
- Hallowell, S., Myers, A.T., Arwade, S.R., 2016. Variability of breaking wave characteristics and impact loads on offshore wind turbines supported by monopiles. *Wind Energy* 19, 301–312.
- Hansen, H.F., Kofeod-Hansen, H., 2017. An engineering-model for extreme wave-induced loads on monopile foundations. In: *Proceedings of the 27th International Conference on Offshore Mechanics and Arctic Engineering (ISOPE) 2017*. <http://dx.doi.org/10.1115/OMAEO2017-62317>.
- Hansen, H.F., Randell, D., Zeeberg, A.R., Jonathan, P., 2020. Directional-seasonal extreme value analysis of North Sea storm conditions. *Ocean Eng.* 195 (September 2019), 106665. <http://dx.doi.org/10.1016/j.oceaneng.2019.106665>, URL <https://linkinghub.elsevier.com/retrieve/pii/S002980181930784X>.
- Hildebrandt, A., Schlurmann, T., 2012. Breaking wave kinematics, local pressures, and forces on a tripod structure. In: *Coastal Engineering Proceedings. Vol. 1*, <http://dx.doi.org/10.9753/icce.v33.structures.71>, URL <http://journals.tdl.org/icce/index.php/icce/article/view/6878>.
- Huang, N.E., Shen, Z., Long, S.R., Wu, M.C., Snin, H.H., Zheng, Q., Yen, N.C., Tung, C.C., Liu, H.H., 1998. The empirical mode decomposition and the hubert spectrum for nonlinear and non-stationary time series analysis. *Proc. R. Soc. A* 454, 903–995. <http://dx.doi.org/10.1098/rspa.1998.0193>.
- Irschick, K., Sparboom, U., Oumeraci, H., 2004. Breaking wave loads on a slender pile in shallow water. In: *Coastal Engineering Proceedings*. pp. 568–580. http://dx.doi.org/10.1142/9789812701916_0045.
- Irschick, K., Schimmels, S., Oumeraci, H., 2011. Breaking criteria for laboratory experiments based on the phase-time-method (ptm). In: *Coastal Engineering Proceedings. Vol. 1*, (32), <http://dx.doi.org/10.9753/icce.v32.waves.6>.
- Jose, J., Choi, S.-j., Lee, K.-h., Gudmestad, O.T., 2016a. Breaking wave forces on an offshore wind turbine foundation (jacket type) in the shallow water. In: *Proceeding of the Twenty-Sixth International Ocean and Polar Engineering Conference (ISOPE) 2016*.
- Jose, J., Podražka, O., Obhrai, C., Gudmestad, O.T., Cieślakiewicz, W., 2016b. Methods for analysing wave slamming loads on truss structures used in offshore wind applications based on experimental data. *Int. J. Offshore Polar Eng.* 26, 100–108. <http://dx.doi.org/10.17736/ijope.2016.mk05>.
- Liu, S., 2019. *CFD modelling of violent breaking wave impacts on marine structures*. (Ph.D. thesis). University of Stavanger, Norway.
- Longuet-Higgins, M.S., 1969. On wave breaking and the equilibrium spectrum of wind-generated waves. *Proc. R. Soc. Lond. Ser. A Math. Phys. Eng. Sci.* 310 (1501), 151–159.
- Miles, M.D., Funke, E.P., 1989. A comparison of methods for synthesis of directional seas. *J. Offshore Mech. Arct. Eng.* 111 (1), 43–48. <http://dx.doi.org/10.1115/1.3257137>.
- Östman, A., Pákozdi, C., Stansberg, C.T., Fagertun, J.T., Vestbøstad, T.M., 2015. CFD simulation and validation of breaking wave impact events in irregular sea states. In: *Proceedings of the Twenty-Fifth International Ocean and Polar Engineering Conference (ISOPE) 2015*. URL <https://onepetro.org/ISOPEIOPEC/proceedings-pdf/ISOPE15/All-ISOPE15/ISOPE-I-15-649/1335434/isope-i-15-649.pdf>.
- Paulsen, B.T., de Sonnevill, B., van der Meulen, M., Jacobsen, N.G., 2018. Probability of wave slamming and the magnitude of slamming loads on offshore wind turbine foundations. *Coast. Eng.* 143, 76–95. <http://dx.doi.org/10.1016/j.coastaleng.2018.10.002>.
- Pierella, F., Bredmose, H., Dixen, M., 2021a. Generation of highly nonlinear irregular waves in a wave flume experiment: Spurious harmonics and their effect on the wave spectrum. *Coast. Eng.* 164, 103816. <http://dx.doi.org/10.1016/j.coastaleng.2020.103816>, URL <https://www.sciencedirect.com/science/article/pii/S0378383920305020>.
- Pierella, F., Bredmose, H., Dixen, M., Ghadirian, A., 2021b. Numerical reproduction of the DeRisk physical model tests on a bottom-fixed foundation exposed to uni- and multi-directional storm sea states. In: *Proceedings of the 40th International Conference on Offshore Mechanics and Arctic Engineering (ISOPE) 2021*. <http://dx.doi.org/10.1115/OMAEO2021-65526>, [arXiv:https://asmedigitalcollection.asme.org/OMAE/proceedings-pdf/OMAEO2021/85116/V001T01A038/6768918/v001t01a038-omae2021-65526.pdf](https://arxiv.org/abs/https://asmedigitalcollection.asme.org/OMAE/proceedings-pdf/OMAEO2021/85116/V001T01A038/6768918/v001t01a038-omae2021-65526.pdf).
- Pierella, F., Ghadirian, A., Bredmose, H., 2019. Extreme wave loads on monopile substructures: Precomputed kinematics coupled with the pressure impulse slamming load model. In: *Proceedings of the ASME Second International Offshore Wind Technical Conference (IOWTC) 2019. American Society of Mechanical Engineers*, <http://dx.doi.org/10.1115/IOWTC2019-7618>, https://asmedigitalcollection.asme.org/OMAE/proceedings/IOWTC2019/59353/St.Julian's_Malta/1071995.
- Pierella, F., Lindberg, O., Bredmose, H., Bingham, H.B., Read, R.W., Engsig-Karup, A.P., 2021c. The DeRisk database: Extreme design waves for offshore wind turbines. *Mar. Struct.* 80, 103046. <http://dx.doi.org/10.1016/j.marstruc.2021.103046>, URL <https://www.sciencedirect.com/science/article/pii/S0951833921001015>.
- Sørensen, J.V.T., Hansen, H.F., Mandviwalla, X., Pierella, F., Bredmose, H., 2021. Direct and fast probabilistic assessment of long term monopile load distribution from combined meteocean data and fully nonlinear wave kinematics. *J. Phys. Conf. Ser.* 2018 (1), 012037. <http://dx.doi.org/10.1088/1742-6596/2018/1/012037>.

- Spinosa, E., Iafrati, A., 2022. A noise reduction method for force measurements in water entry experiments based on the ensemble empirical mode decomposition. *Mech. Syst. Signal Process.* 168, 108659. <http://dx.doi.org/10.1016/J.YMSSP.2021.108659>, URL <http://arxiv.org/abs/2109.14310>.
- Stansberg, C., Huse, E., Krokstad, J., Lehn, E., 1995. Experimental study of non-linear loads on vertical cylinders in steep random waves. In: Proceedings of the Fifth International Ocean and Polar Engineering Conference (ISOPE) 1995. URL <https://onepetro.org/ISOPEIOPEC/proceedings-pdf/ISOPE95/All-ISOPE95/ISOPE-1-95-013/1963669/isope-i-95-013.pdf>.
- Suja-Thauvin, L., Krokstad, J.R., Bachynski, E.E., de Ridder, E.J., 2017. Experimental results of a multimode monopile offshore wind turbine support structure subjected to steep and breaking irregular waves. *Ocean Eng.* 146, <http://dx.doi.org/10.1016/j.oceaneng.2017.09.024>.
- Sumer, B.M., Fredsøe, J., Sumer, M., Fredsoe, J., 2006. *Hydrodynamics Around Cylindrical Structures*, first ed. World Scientific Publishing Company, p. 550.
- Veic, D., Sulisz, W., 2018. Impact pressure distribution on a monopile structure excited by irregular breaking wave. *Pol. Marit. Res.* 25, 29–35. <http://dx.doi.org/10.2478/pomr-2018-0019>, URL <https://content.sciendo.com/doi/10.2478/pomr-2018-0019>.
- Vestbøstad, T.M., Økland, O.D., Lian, G., Stavang, T.P., 2017. Column slamming loads on a TLP from steep and breaking waves. In: Proceedings of the Seventeenth International Conference on Offshore Mechanics and Arctic Engineering (ISOPE) 2017. <http://dx.doi.org/10.1115/OMAE2017-61786>, URL <https://asmedigitalcollection.asme.org/OMAE/proceedings-pdf/OMAE2017/57632/V001T01A064/2532574/v001t01a064-omae2017-61786.pdf>.
- von Karman, T., 1929. The impact on seaplane floats during landing.
- Wagner, H., 1932. Über stoß-und gleitvorgänge an der oberfläche von flüssigkeiten. *ZAMM Z. Angew. Math. Mech.* 12 (4), 193–215.
- Walker, D.A.G., Taylor, P.H., Eatock Taylor, R., 2004. The shape of large surface waves on the open sea and the Draupner new year wave. *Appl. Ocean Res.* 26 (3–4), 73–83. <http://dx.doi.org/10.1016/j.apor.2005.02.001>.
- Wienke, J., Oumeraci, H., 2005. Breaking wave impact force on a vertical and inclined slender pile - Theoretical and large-scale model investigations. *Coast. Eng.* 52, 435–462. <http://dx.doi.org/10.1016/j.coastaleng.2004.12.008>.